

University of Nebraska - Lincoln

DigitalCommons@University of Nebraska - Lincoln

Mechanical (and Materials) Engineering --
Dissertations, Theses, and Student Research

Mechanical & Materials Engineering,
Department of

Summer 7-31-2010

Structural and Magnetic Properties of Neodymium - Iron - Boron Clusters

Jeremy J. Anderson

University of Nebraska at Lincoln, anderson.jeremy.j@gmail.com

Follow this and additional works at: <https://digitalcommons.unl.edu/mechengdiss>



Part of the [Mechanical Engineering Commons](#), [Metallurgy Commons](#), and the [Other Materials Science and Engineering Commons](#)

Anderson, Jeremy J., "Structural and Magnetic Properties of Neodymium - Iron - Boron Clusters" (2010).
Mechanical (and Materials) Engineering -- Dissertations, Theses, and Student Research. 10.
<https://digitalcommons.unl.edu/mechengdiss/10>

This Article is brought to you for free and open access by the Mechanical & Materials Engineering, Department of at DigitalCommons@University of Nebraska - Lincoln. It has been accepted for inclusion in Mechanical (and Materials) Engineering -- Dissertations, Theses, and Student Research by an authorized administrator of DigitalCommons@University of Nebraska - Lincoln.

STRUCTURAL AND MAGNETIC PROPERTIES OF NEODYMIUM – IRON - BORON
CLUSTERS

by

Jeremy J. Anderson

A THESIS

Presented to the Faculty of

The Graduate College at the University of Nebraska

In Partial Fulfillment of Requirements

For the Degree of Master of Science

Major: Mechanical Engineering

Under the Supervision of Professor Jeffrey E. Shield

Lincoln, Nebraska

August, 2010

Table of Contents

1	Introduction.....	1
1.1	Objectives	2
2	Magnetic Materials	3
2.1	Magnetic Origins	3
2.2	Magnetism.....	4
2.2.1	Ferromagnetism	6
2.3	Hysteresis.....	7
2.4	Domains	9
2.4.1	Single Domains	12
2.5	Soft Magnetic Materials.....	15
2.6	Hard Magnetic Materials	15
2.6.1	High Energy Hard Magnetic Materials	17
2.6.2	Thin Film Nd ₂ Fe ₁₄ B	20
3	Experimental Techniques.....	22
3.1	Sputtering.....	22
3.1.1	Clusters	23
3.1.2	Cluster Process.....	24
3.1.3	Sputtering Yields of Alloy Targets	26
3.1.4	Impact Dynamics	26
3.2	Mass Selector	28
3.3	X-Ray Diffraction	28
3.4	Alternating Gradient Force Magnetometer	30
3.5	Transmission Electron Microscope.....	30
3.5.1	Selected Area Diffraction.....	31
3.5.2	Energy Dispersive Spectroscopy	31
3.6	Superconducting Quantum Interference Device (SQUID)	31
4	Experimental Procedures.....	33
4.1	Nd ₂ Fe ₁₄ B Target.....	34
4.2	Cluster Deposition using a (Fe-Co)-Nd-B Target.....	35
5	Results and Discussion.....	37

5.1	As Deposited Clusters.....	37
5.2	Annealing.....	46
6	Conclusions.....	54
7	Works Cited.....	55

Table of Figures

Figure 2-1: (a) Magnetic moment created by the electron orbit around a nucleus. (b) Magnetic moment created by electron spin. [3].....	3
Figure 2-2: Atomic dipole configuration of a diamagnetic field with and without an external magnetic field (H) applied. [2].....	4
Figure 2-3: Atomic dipole configuration of a paramagnetic field with and without an external magnetic field. [2].....	5
Figure 2-4: Illustration of antiferromagnetic material, demonstrating antiparallel spin alignment which cancels the net magnetic moment of the material. [2].....	6
Figure 2-5: Illustration of the mutual alignment of dipoles, exhibited by ferromagnetic materials in the absence of an external magnetic field. [2]	7
Figure 2-6: Important features of the ferromagnetic hysteresis loop. [3]	8
Figure 2-7: Structure of 180° domain wall between two domains in opposite alignment. [3]	9
Figure 2-8: The domain behavior during the stages of magnetization and demagnetization, shown at several points along the hysteresis loop. [2]	10
Figure 2-9: Magnetostatic energy dependence on particle size and number of domains. The multi-domain curve will vary depending on the number of domains present. [3]	13
Figure 2-10: The effect of decreasing particle size on coercivity. D_s is the ideal particle size with a single domain and maximum coercivity. Below D_p the particles become unstable and superparamagnetic. [3].....	14
Figure 2-11: Comparison of the hysteresis loops of hard and soft magnetic material. Hard materials have a higher coercivity while soft materials have a higher saturation magnetization. [2]	16
Figure 2-12: Crystal structure of tetragonal Nd ₂ Fe ₁₄ B. [7].....	18
Figure 2-13: Nd-Fe-B three phase diagram [8].....	19

Figure 2-14: The Nd-Fe phase diagram [9]	20
Figure 3-1: During sputtering an ionized particle collides with the target surface releasing target atoms. [13]	23
Figure 3-2: A magnetron sputtering device contains magnets located directly behind the target. The target is kept cool by a running water supply. [14]	25
Figure 3-3: Deposition of clusters at various voltages. Clusters with low sputtering energy deposit on a substrate and retain their shape. Clusters with high sputtering voltages fragment and create thin films when deposited. [19]	27
Figure 3-4: Diagram of quadrupole mass analyzer filtering ionized particles. Stable particle of desirable mass are accelerated through the device. Unstable particle of undesirable mass collide with the poles or are lost in the system. [22]	28
Figure 3-5: Diffraction of x-rays in a crystal lattice. X-rays will diffract off parallel planes according to Bragg's law. [23]	29
Figure 4-1: The cluster system at UNL. Clusters are created at the rightmost DC magnetron sputtering source and deposited onto substrates at the sample holder. The upper and lower sputtering sources can be used to create thin films on the sample.	33
Figure 4-2: The composite sputtering target. The inner plugs of material follow the racetrack created during sputtering	34
Figure 5-1: Composite target used during deposition. The racetrack as well as the plugs has been outlined	37
Figure 5-2: As-deposited clusters with an average diameter of 8.1 nm (left) as seen from bright field TEM. The diffraction pattern (right) from the clusters shows diffuse rings indicating amorphous structures.	38
Figure 5-3: The AGFM data of as-deposited clusters from the composite target	39
Figure 5-4: TEM image of as-deposited clusters used for size analysis.	40
Figure 5-5: The distribution of cluster sizes from five TEM bright field images	41

- Figure 5-6:** A film of as-deposited amorphous clusters approximately 15nm thick. The diffraction pattern (inset) shows diffuse rings confirming clusters are amorphous..... 42
- Figure 5-7:** EDS spectrum of cluster material. Copper is present from the TEM grid. Carbon was used to cap the clusters. Oxygen indicates some of the sample has become oxidized. 43
- Figure 5-8:** The SQUID analysis of as-deposited cluster material at 300 K (upper graph) and 0 K (lower graph) shows superparamagnetic properties at high temperatures and ferromagnetic properties at low temperatures..... 45
- Figure 5-9:** AGFM data of the as-deposited cluster material. The hysteresis loop shows a soft-magnetic material..... 46
- Figure 5-10:** AGFM data of annealed cluster material. The clusters were annealed for four minutes at 600oC. 47
- Figure 5-11:** The dependence of coercivity as a result of annealing time. Samples were annealed at 600oC in an inert gas atmosphere. 48
- Figure 5-12:** The dependence of coercivity at different annealing temperatures with increasing time. 49
- Figure 5-13:** The SQUID analysis of annealed cluster material at 300 K (upper graph) and 0 K (lower graph). There is a moderate increase in coercivity at low temperatures..... 50
- Figure 5-14:** TEM image of a thin film of annealed clusters approximately 15 nm thick. Sintering has occurred between cluster particles. 51
- Figure 5-15:** Indexed SAD patterns of cluster samples. The bcc-Nd is shown in red and Nd₂Fe₁₇ is shown in blue..... 52

1 Introduction

For thousands of years, magnets were used merely as toys and compass needles. Since the advent of electronics, magnets have found their use in many everyday objects. Beginning in the 20th century many advances were made in magnetic materials. Magnets are now used widely in electric motors, speakers, turbines, hard drives, cathode ray tubes, credit cards, magnetic resonance imaging devices, transformers and more.

Alnico magnets were some of the first magnetic materials produced. These were made up of aluminum, nickel and cobalt. Compared to today's standards these had poor magnetic properties, but overall good temperature properties. Ceramic and ferrite magnets were developed in the early 1950's. These are what are commonly found on refrigerators today. The 1960's saw the creation of samarium cobalt magnets, which had the highest energy product of any magnetic material. Due to an increase in the cost of cobalt, there began a large push for an iron-based permanent magnet. Soon after, in the 1980's, neodymium-iron-boron magnets were developed with the largest energy product. Since the discovery of neodymium-iron-boron, few advances have been made in magnetic materials [1].

With advances in thin film deposition processes and sputtering technologies, more research is being done to create magnetic materials with enhanced properties. Exchange-spring permanent magnetic materials aim to accomplish this goal. Combining soft and hard magnetic materials at the nano-scale level can enhance remanence, coercivity, and energy products of magnetic materials. Recently, progress has been made on exchange-coupled Fe/FePt with energy products 70% greater than expected [2]. The magnetic properties of these depend heavily on uniform, nano-scale soft magnetic phases. Decreasing the cluster size creates single domain particles with a greater energy product [2].

1.1 Objectives

The main objective of this investigation was the creation of clusters of $\text{Nd}_2\text{Fe}_{14}\text{B}$. The primary purpose was to create isolated single domain particles of uniform size and shape to obtain a magnetic material with a high energy product.

2 Magnetic Materials

2.1 Magnetic Origins

Magnetic moments are the result of electron motion, electron spin, and nuclear magnetic moment. Each electron in an atom contributes to the magnetic moment. A magnetic field is generated from the electron's orbital motion around the nucleus as seen in Figure 2-1(a). A magnetic moment is also generated along the electron's axis of rotation created from the spin of the nucleus as seen in Figure 2-1(b). The greater the forces aligning any spin in a region, the greater the degree of spin alignment in that particular region, and thus a greater overall magnetization [3].

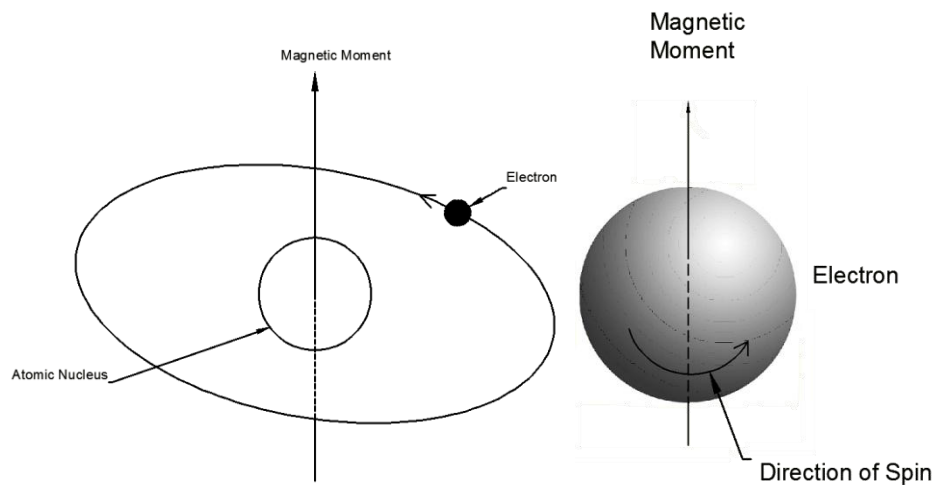


Figure 2-1: (a) Magnetic moment created by the electron orbit around a nucleus. (b) Magnetic moment created by electron spin. [1]

The magnitude of the internal field strength within the substance is known as the magnetic induction and is denoted by 'B'. The magnetic field strength is denoted by 'H'. The magnetic induction and magnetic field strength are related by the following equation.

$$B = \mu H \quad (2-1)$$

The variable μ is the permeability specific to the medium through which the H field passes [3].

Magnetic permeability is a measure of the magnetization a material obtains as a response to an applied magnetic field. Permeability is dependent on the material, with the permeability of diamagnetic materials being less than one and the permeability of ferromagnets being much greater than one [3].

2.2 Magnetism

Diamagnetic materials have the unique property of creating magnetic fields in direct opposition of the applied magnetic field. Diamagnetism is a weak form of magnetism, all materials exhibit a diamagnetic signal, but it is weak and easily washed out by stronger signals. Diamagnetism persists only while an external field is present. The external field changes the orbital motions of the electrons, creating a magnetic field in the opposite direction [3]. When a diamagnetic material is placed between the poles of a strong electromagnet, the material is attracted to weak regions in the field.

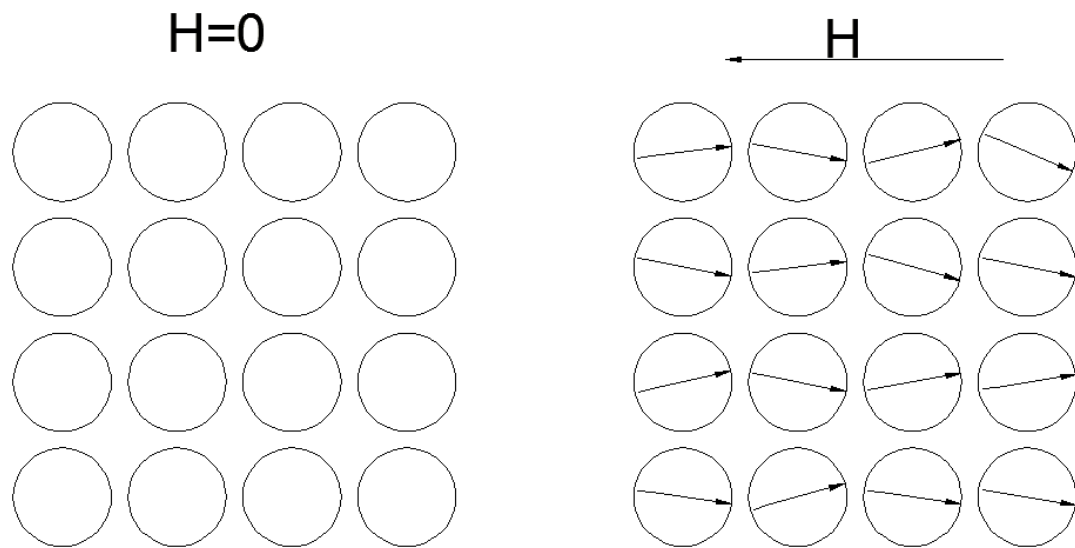


Figure 2-2: Atomic dipole configuration of a diamagnetic field with and without an external magnetic field (H) applied. [3]

Diamagnetic materials are typically those which are considered non-magnetic. Most organic compounds fall in this classification, as well as many metals such as copper, mercury, and gold. Metals which are typically diamagnetic are heavy metals with core electrons.

In paramagnetic materials, each atom possesses a permanent dipole moment, resulting from incomplete cancellation of the electron spins or orbital magnetic moments. These atomic magnetic moments are randomly oriented. Paramagnetic material has no net macroscopic magnetization and exhibit magnetic behavior only in the presence of a magnetic field and retains no magnetism when the field is removed. The dipoles of paramagnetic materials do not affect the surrounding dipoles within the material [3].

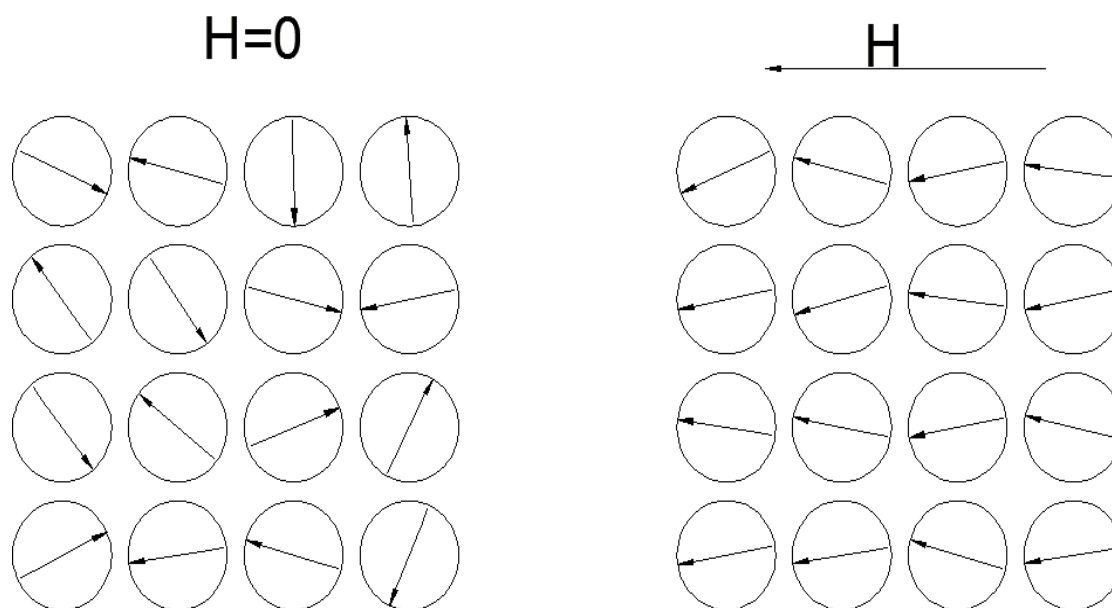


Figure 2-3: Atomic dipole configuration of a paramagnetic field with and without an external magnetic field. [3]

Antiferromagnetic materials possess no net magnetic moment and exhibit a magnetic moment coupling which is anti-parallel. Neighboring ions' dipoles are in exactly the opposite direction of one another (Figure 2-3) [3].

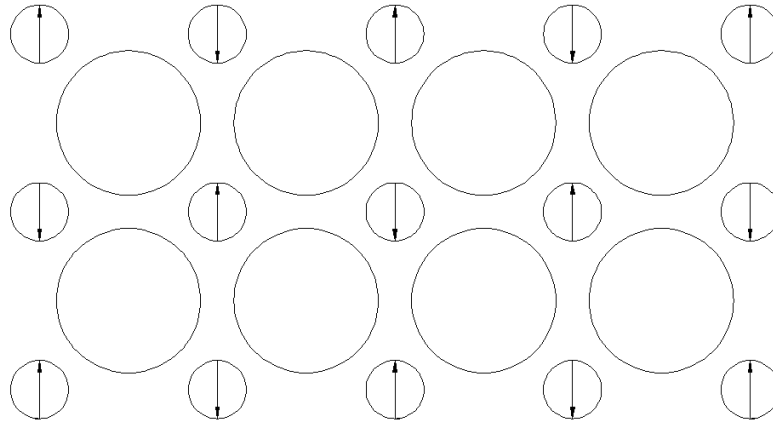


Figure 2-4: Illustration of antiferromagnetic material, demonstrating antiparallel spin alignment which cancels the net magnetic moment of the material. [3]

Ionically bonded materials that exhibit permanent magnetization are ferrimagnets. Ferrimagnetic materials exhibit a magnetic moment from the incomplete cancelation of ion spin moments. Saturation magnetizations for ferrimagnetic materials are not as high as those for ferromagnets. Since ferrimagnets are ceramic materials, they are good for use as electrical insulators [3].

2.2.1 Ferromagnetism

Ferromagnetic materials are those which produce a magnetic moment in the absence of external fields and are capable of large permanent magnetizations. In ferromagnetic material, there are coupling interactions which cause adjacent moments to align with one another in the absence of an external field. The alignment exists in volume regions known as magnetic domains [3].

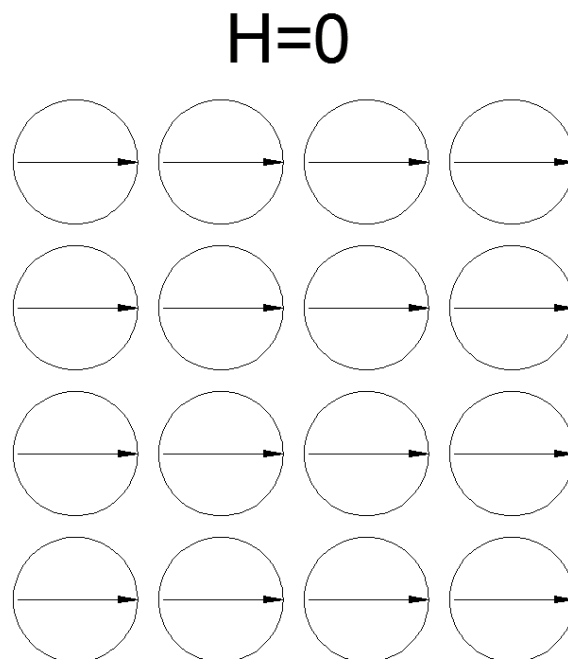


Figure 2-5: Illustration of the mutual alignment of dipoles, exhibited by ferromagnetic materials in the absence of an external magnetic field. [3]

When a large enough external field is applied to a magnetic material, the magnetization (M) becomes constant, aligning all domains within the magnet, causing it to become saturated. The saturation magnetism is the maximum possible magnetization of a material resulting when each individual dipole is aligned [3].

Ferromagnetic materials typically have a preferred direction of magnetization. In this direction, magnetization is the easiest, and it is also the strongest. Saturation can easily be attained in the easy directions [3].

2.3 Hysteresis

As a magnetic field is applied and the strength of it increased, the domains of the material change size and shape by the movement of the domain boundaries. In fields of high magnetic strength, the magnetization becomes constant or saturated, known as the saturated magnetism. From the saturation point, as the field is reduced by reversal of the field direction, the curve does

not retrace its original path. When the magnetic field strength is reduced to zero after saturation, the material will remain magnetized. This magnetization is referred to as the remanence.

Materials in which the magnetization does not reduce to zero when the applied magnetic field is reduced to zero are permanent magnets. If the applied field is reversed, the remaining induction will decrease to zero when the reverse field equals the coercivity. The area within a loop represents the energy loss per unit volume of material during the demagnetization process which appears as heat generated within the material (see Figure 2-6). The energy product of the magnet is represented by the maximum area formed in the second quadrant ($BH\text{-max}$) [1].

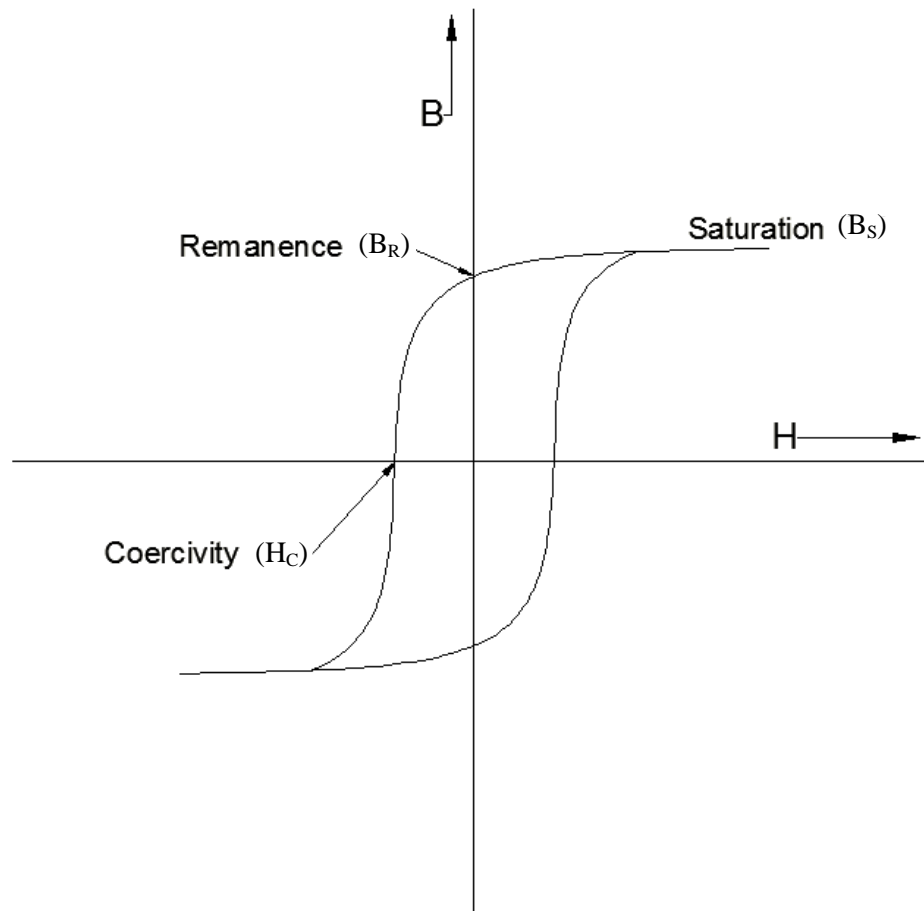


Figure 2-6: Important features of the ferromagnetic hysteresis loop. [1]

2.4 Domains

In ferromagnetic and ferrimagnetic materials, there are regions in which there are mutual alignments of dipole moment known as a magnetic domain. The exchange energy is at a minimum when spins in adjacent domains are parallel to one another; likewise spins in opposite directions will have the maximum exchange energy. Adjacent domains are separated by domain boundaries and within these boundaries the magnetization gradually changes. When adjacent atoms within the domain boundary progressively change, allowing the spins to gradually change over 180° (Figure 2-7), there is a reduction in the exchange energy.

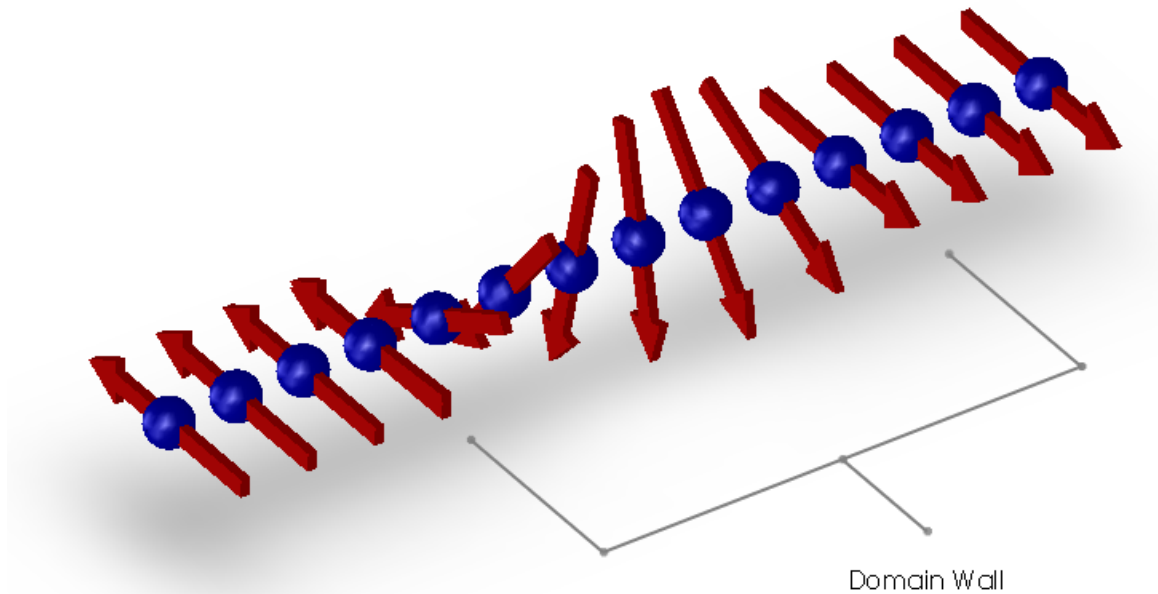


Figure 2-7: Structure of 180° domain wall between two domains in opposite alignment. [1]

Spins in adjacent domains magnetized in easy directions will have domain boundaries in which the spins will be oriented in non-easy directions, creating higher crystal anisotropy. The magnitude of the magnetic field in multi-domain material is the vector sum of the magnetizations of all the domains. Domains separated by 180° magnetic moments are known as Bloch walls with a thickness δ_B and are described by the below equation where A is the exchange stiffness [4].

$$\delta_B = \pi \sqrt{\frac{A}{K}} \quad (2-2)$$

In bulk specimens, the wall thickness is much smaller than the specimen. The exchange energy and the anisotropy of the material contribute to the domain wall width and structure. The exchange energy tends to create larger domain boundaries by creating smaller angles that are made by adjacent spins within the boundary. The anisotropy energy reduces the domain wall thickness by reducing the number of atoms with axes in non-easy directions [1].

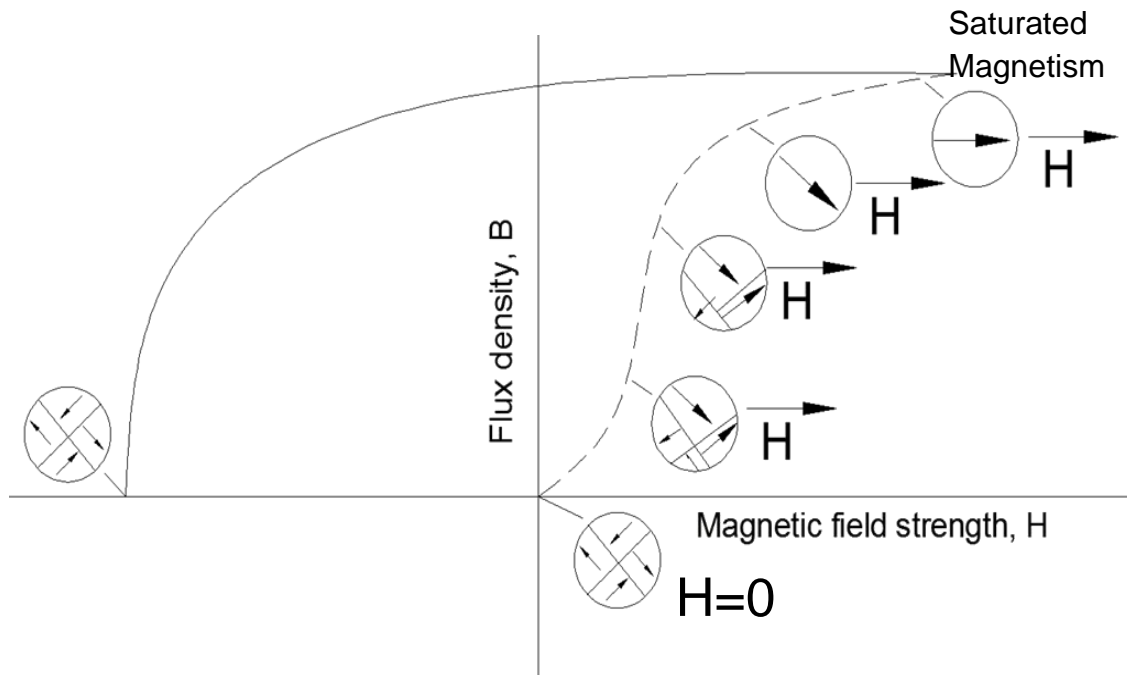


Figure 2-8: The domain behavior during the stages of magnetization and demagnetization, shown at several points along the hysteresis loop. [3]

The domain structure changes through domain wall movement as the magnetic field strength changes, illustrated in figure (2-8). As a magnetic material approaches saturation magnetism there is a movement in the domain walls resulting in a final domain structure with the direction of magnetization in the same direction as the applied field.

The domain wall structures of magnetic materials can vary depending on the material. Bloch walls are typically encountered in bulk materials, in which these boundaries show a gradual shift in the reversal of magnetization vectors. In thin film materials, the domain boundaries have the possibility of forming a special type of domain boundary with an axis of rotation of the moments through the wall not equal to 180° , termed a Néel wall. The shape of the domain wall depends greatly on the wall favoring the lowest energy. The magnetostatic energy density of the Bloch and Néel walls are given by equations 2-3 and 2-4 respectively [4].

$$E_B = 2\pi\delta^2 M_S^2 (t + \delta)^{-1} \quad (2-3)$$

$$E_N = 2\pi t \delta M_S^2 (t + \delta)^{-1} \quad (2-4)$$

Where δ is the domain wall thickness, t is equal the film thickness, and M_S is the saturation magnetization.

In the absence of domain structure, a high coercivity must result in order to produce this coercivity, anisotropy must also be present. The presence of anisotropy in any material creates a preferred direction of magnetization [1].

Permanent magnets tend to be mainly categorized with a high degree of shape or crystal anisotropy. Columnar shaped crystals have the highest coercivities and therefore make the best permanent magnets. The columns stack upon one another, further increasing the coercivity of the bulk material.

2.4.1 Single Domains

Single-domain particles are of great interest in magnetic research having only one domain means that, upon reversal of the magnetic field, there is a rotation of the magnetic moment. The rotation of the magnetic moment in turn causes the rotation of the particle. This rotation is only possible if the anisotropy forces (such as crystal, shape, and stress) of the entire system are overcome.

In single domain systems, some anisotropy must be present to produce a high coercivity. The anisotropy produces a preferred direction of magnetization and results from magnetocrystalline anisotropy, strain anisotropy, or shape anisotropy. The hysteresis loop shape that results from this anisotropy is based largely on the particle orientation [1].

A crystal will often spontaneously adopt multiple domains to reduce the magnetostatic energy. The ratio of energies between a single domain and multi-domain crystal is described by equation (2-5). The ratio of energies varies by \sqrt{L} , where L is the crystal thickness. When L becomes very small, the crystal will tend to remain in the single domain state. [1]

$$\frac{E(\text{single-domain crystal})}{E(\text{multi-domain crystal})} = \frac{2\pi M_S^2 L}{2\sqrt{1.7M_S^2 \gamma L}} = 2.4\sqrt{\frac{M_S^2 L}{\gamma}} \quad (2-5)$$

If a cubic crystal has closure domains, the resulting magnetostatic energy will be zero. The total resulting energy results from the wall energy, which varies with the wall area, L^2 . If a crystal is uniaxial, the total energy will be the sum of the magnetostatic energy and the wall energy. If the energy for a single-domain crystal and the energy for a multi-domain crystal are equated, the resulting equation can be solved for a critical value of L (equation 2-6). [1]

$$L_c = \frac{1.7\gamma}{\pi^2 M_S^2} \quad (2-6)$$

It is possible for the value of L_C to be less than the domain wall thickness in some materials. It is not possible to reduce the magnetostatic energy of the particle by the creation of another domain. If a domain wall was to form, the wall would need to be so thin enough that the energy created by the wall would exceed the decrease in magnetostatic energy of the particle. [1]

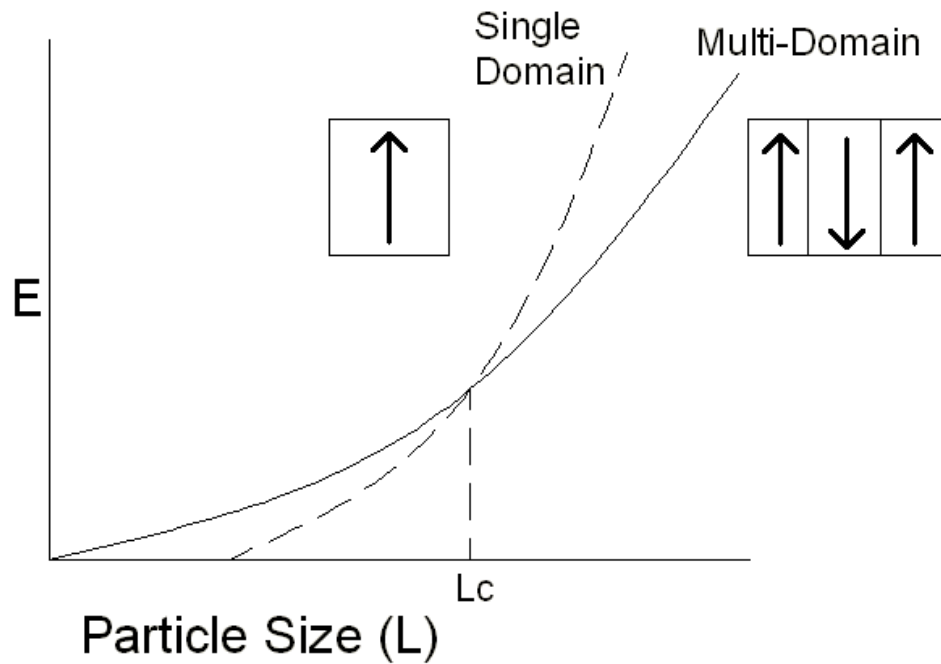


Figure 2-9: Magnetostatic energy dependence on particle size and number of domains. The multi-domain curve will vary depending on the number of domains present. [1]

Domain wall motion changes the magnetic behavior of the material in single-domain systems. There is a size dependence on the coercivity and it has been experimentally found to be approximated by the following equation, in which g and h are material dependent and D is the particle diameter [1].

$$H_{ci} = g + \frac{h}{D^{3/2}} \quad (2-7)$$

Single domain particles exist below a critical diameter D_s . At the critical diameter there is a maximum value of coercivity. Particles of critical size and smaller change the direction of their dipole by changing their atomic spin rotation. Particles below the critical diameter D_s experience

a loss in coercivity due to thermal effects and an exchange interaction through grain surfaces. Smaller grain sizes result in a stronger interaction through grain surfaces due to an increase in the ratio of surface area to volume. Coercivity tends to zero with decreasing particle diameter until it reaches a critical particle diameter D_p after which the coercivity remains constant at zero (see Figure 2-10). The magnetic properties of particles result from forces of shape and crystal anisotropy [1].

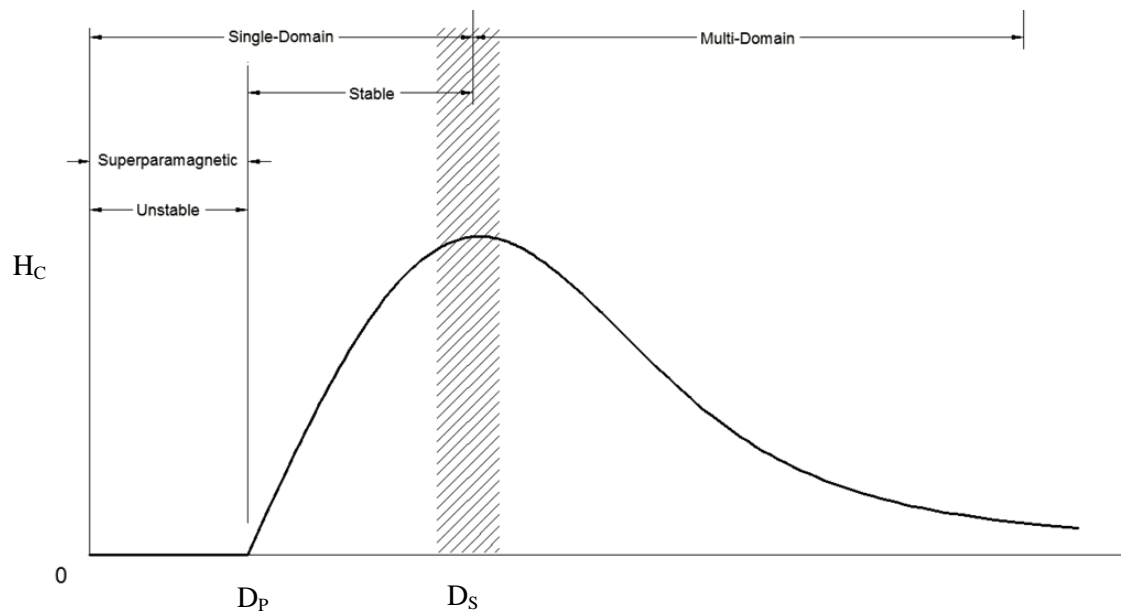


Figure 2-10: The effect of decreasing particle size on coercivity. D_s is the ideal particle size with a single domain and maximum coercivity. Below D_p the particles become unstable and superparamagnetic. [1]

2.5 Soft Magnetic Materials

Soft magnetic materials are used in areas subjected to alternating magnetic fields. Energy losses in soft magnetic materials are low, which can be seen by the minimal area occupied by the hysteresis loop. A low coercivity is caused by the movement of domain walls. Voids and non-magnetic particle inclusions can be inserted in soft magnetic particles which will consequently increase the coercivity by the hindrance of domain wall motion. Additionally domain walls are pinned by defects such as dislocations, magnetostriction, or plastic deformation thereby increasing the coercivity [3].

2.6 Hard Magnetic Materials

Hard magnetic materials are characterized by high coercivity, remanence, saturation flux density, high hysteresis energy losses, as well as low initial permeability. Like soft magnetic materials, restricting domain wall motion will enhance the coercivity of the material. Hard magnetic materials are often desired in numerous applications because they require no external power source and consequently generate no heat during usage. Hard magnets are essentially energy storage devices, which with proper handling, can retain their magnetism [1].

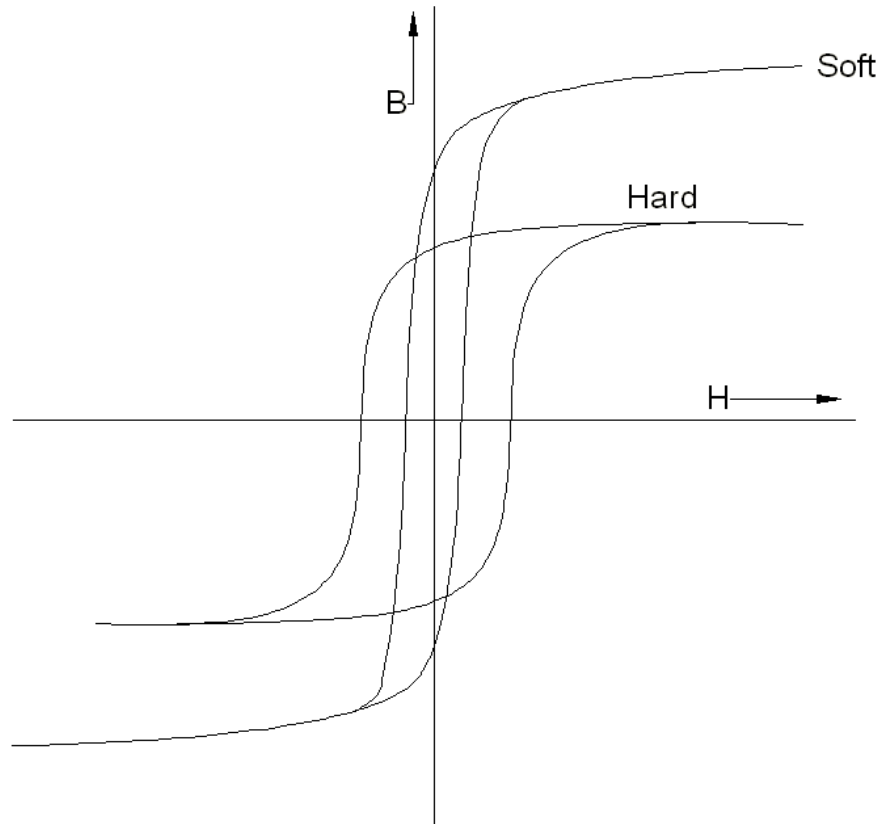


Figure 2-11: Comparison of the hysteresis loops of hard and soft magnetic material. Hard materials have a higher coercivity while soft materials have a higher saturation magnetization. [3]

The coercivity of hard magnetic materials is strongly dependent on the microstructural features of the material. The experimental coercivity is always factors approximately 3-5 times less than the theoretical prediction of the material; this is known as Brown's paradox [5]. This results when particle size increases to the point where the particle can contain domain walls which aid in the nucleation and propagation of reverse domains decreasing the material's coercivity. Likewise, this can also happen in small-grained systems where interactions and microstructural defects make it easier to reverse. For nanocrystalline magnetic materials the coercivity can be explained by the Kronmuller equation (2-5).

$$\mu_0 H_c = \alpha_{ex} \alpha_k \alpha_\psi \mu_0 H_a - N_{eff} J_s \quad (2-8)$$

The parameters α_{ex} , α_k , α_ψ , and N_{eff} are the microstructural parameters. The parameter α_{ex} describes the coupling effect of neighboring grains on the coercivity. The affect of non-perfect grains in which nucleation and pinning is likely to occur is represented by α_k . The reduction of coercivity from the misalignment of grains is given by α_ψ . The effective demagnetization factor is N_{eff} , where J_s is the saturation magnetism.

2.6.1 High Energy Hard Magnetic Materials

High energy magnetic materials are considered to be those with coercivities of about 10 MGOe. Two such materials, neodymium-iron-boron and samarium-cobalt, have been developed commercially for this purpose. High energy magnetic materials are often used in place of electromagnets because they continuously maintain magnetic fields and generate no heat during operation. Permanent magnet motors are often much smaller than electromagnetic motors [3].

Table 1: Magnetic properties of common magnetic materials

Material	At 25°C			At 250°C			Tc (°C)
	Hc (kOe)	iHc (kOe)	(BH)max (MGOe)	Hc (kOe)	iHc (kOe)	(BH)max (MGOe)	
Sm₂Co₁₇	10.69	25	31.5	8.68	10.3	25.4	805
Alnico 5	0.74	0.75	5.3	0.73	75	5.18	840
Nd₂Fe₁₄B	13.7	13.9	45.2	0.63	0.65	1.52	310

2.6.1.1 Neodymium-Iron-Boron Magnets

Samarium-Cobalt magnets are relatively expensive due to the materials involved in manufacturing them. Neodymium-Iron-Boron (Nd₂Fe₁₄B) magnets are widely being used because the materials involved in manufacturing are relatively inexpensive. The coercivities of these rival those of samarium-cobalt magnets while the energy products are far superior.

The crystal structure and symmetry of $\text{Nd}_2\text{Fe}_{14}\text{B}$ result from mirror symmetry in two orthogonal planes and contribute to its strong magnetic properties. The structure of $\text{Nd}_2\text{Fe}_{14}\text{B}$ is tetragonal in structure and has space group symmetry of $P4_2/mnm$; the neodymium and iron are in parallel alignment within the sublattices. This symmetry produces a magnetization of approximately 1.6 T at room temperature and an anisotropy of resulting from the 'mm' symmetry through the two neodymium sites [6].

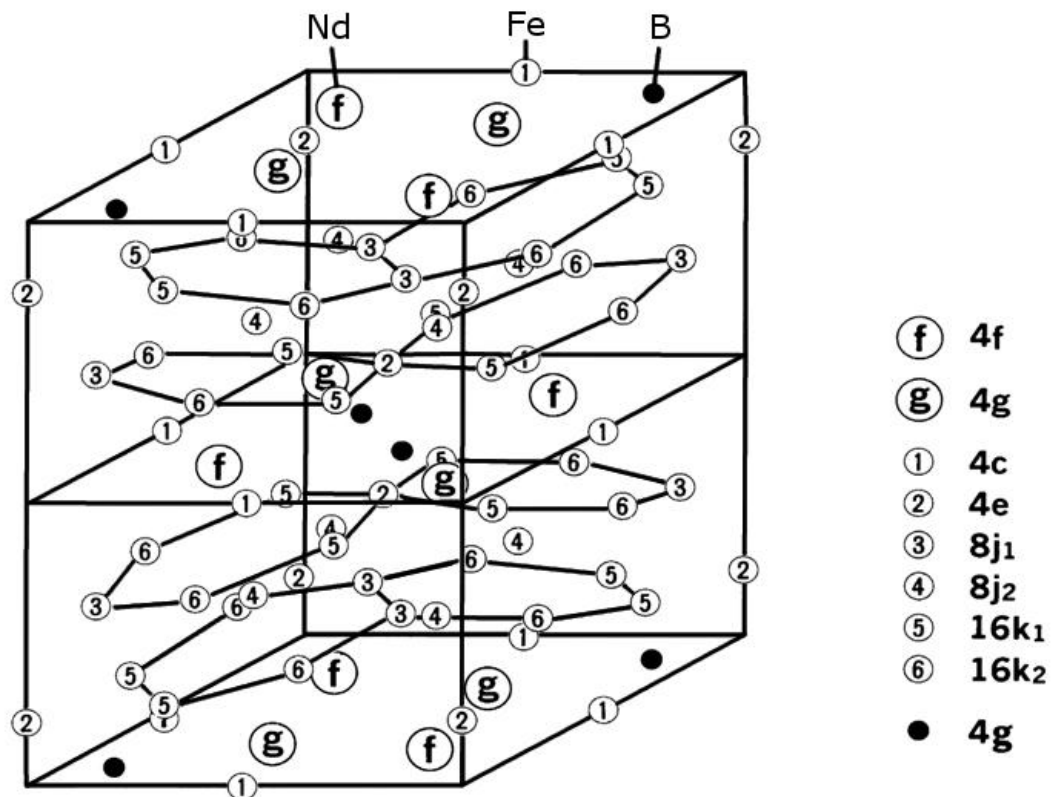


Figure 2-12: Crystal structure of tetragonal $\text{Nd}_2\text{Fe}_{14}\text{B}$. [7]

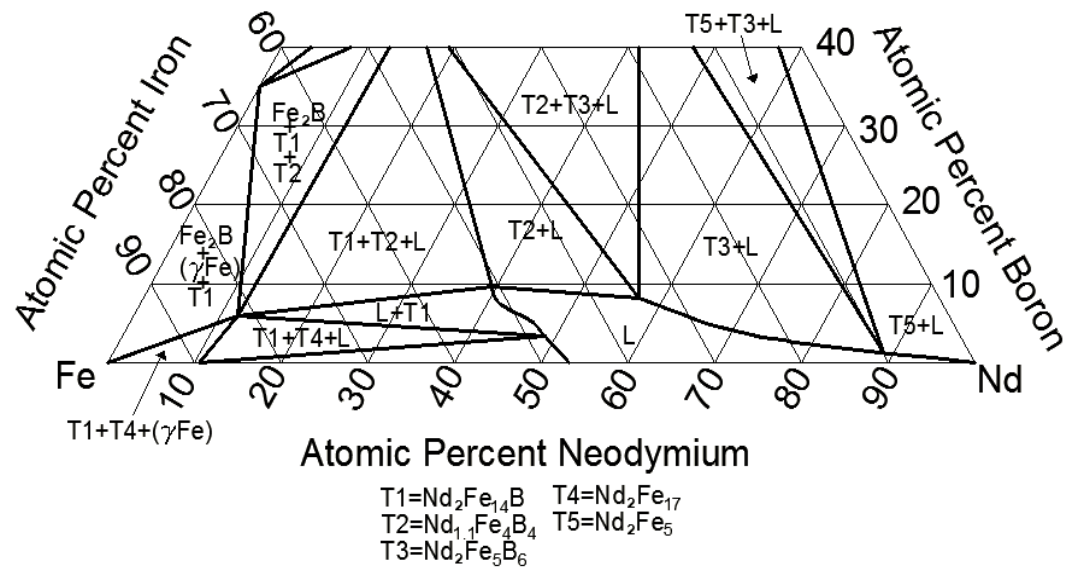


Figure 2-13: Nd-Fe-B three phase diagram [8]

Microstructure plays a crucial role in the magnetic properties of Nd₂Fe₁₄B magnets. The magnetization and demagnetization can be altered by controlling the size, shape, and orientation of the grains. To achieve different microstructures, three different processing techniques are currently employed powdered metallurgical methods-sintering and melt spinning and mechanical alloying [7].

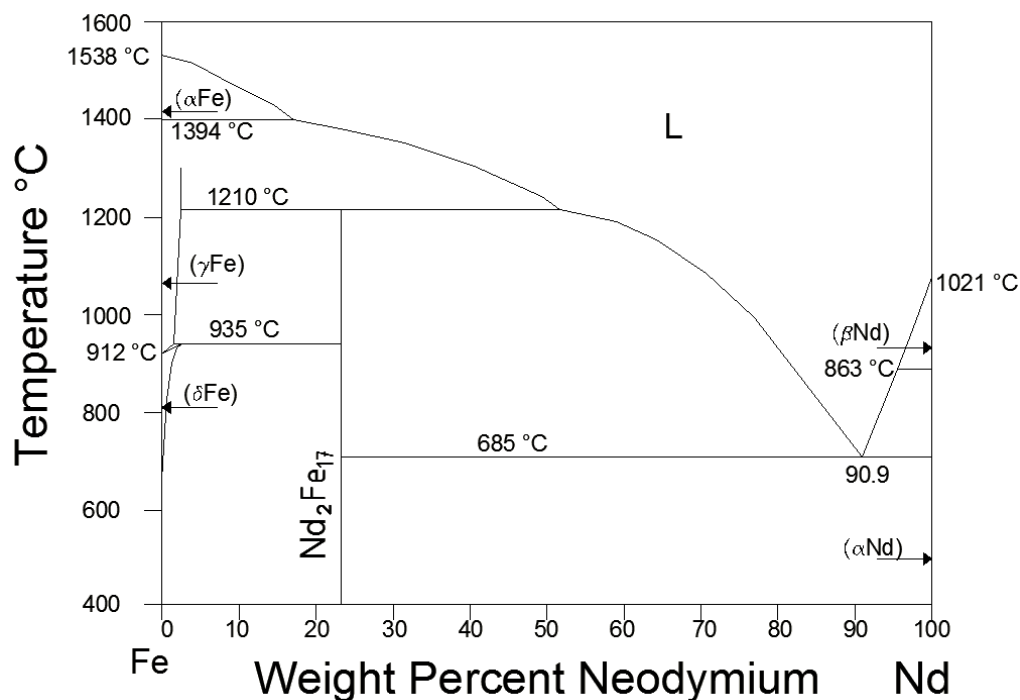


Figure 2-14: The Nd-Fe phase diagram [9]

2.6.2 Thin Film Nd₂Fe₁₄B

With the advent of computers and the dramatic increase in the need to store information, a need has arisen for high density data storage. Recent research in Nd₂Fe₁₄B has been towards the creation of thin films which are highly textured with the easy axis perpendicular to the film plane. Films of this type have the possibility of storage densities of 10-20 Gbit/in² with thicknesses below 100 nm [10]. As well as finding use in data storage, these thin film materials have potential for application in micro-mechanical devices, motors, and actuators.

Research in this area is driven toward creating films of uniform consistency and texture. These films are deposited at low deposition rates and low power densities; depositing films in this fashion creates amorphous films which require either a heated substrate during deposition or secondary annealing. Films deposited close to stoichiometry were found to be deposited at low temperatures whereas films deposited at high temperatures were enriched with Nd [11]. The

buffer layer used to prevent oxidation of the $\text{Nd}_2\text{Fe}_{14}\text{B}$ films is also critical. The choice of a buffer layer thickness and composition has direct effects on the surface morphology [12].

3 Experimental Techniques

The following section covers many of the techniques used in the experiments. The discussion begins with inert gas condensation methods then x-ray diffraction methods, alternating gradient force magnetometer methods, transmission electron microscopy, and finally the superconducting quantum interference device.

3.1 Sputtering

Deposition of thin films has become an extremely important field in technology in recent years, with progress being made in many areas of nano-technology striving for smaller and smaller devices. Evaporation and sputtering have since become well established methods of creating thin films. Sputtering methods, such as radio-frequency and magnetron sputtering, allow for vaporization of the material without the heating of the target material. Cluster-assembled materials can be created from metals, ceramics, semiconductors, or even composites. These structures can consist of nano-scale phases, crystalline, quasicrystalline, or amorphous [13].

Sputter deposition is a series of quasi-elastic collision processes induced by a bombarding ion. Sputtering can be thought of as a multiple collision processes involving a cascade of moving target atoms. When sputtering with a target material, the majority of the atoms are sputtered by random collision processes. The sputtering yield is mostly accounted for by the target's surface atoms [13]. There is a wide range of materials that can be sputtered. However, due to the bombardment process and the vacuum environment, materials such as, organic solids or volatile components can not be sputter deposited [14].

To understand sputtering theory, both transport theory and single collision arguments must be taken into account. During the sputtering process an ion undergoes a series of collisions within the target. Atoms then recoil with sufficient energy to cause secondary collisions, creating

more recoiling atoms. The ion and the energetic recoil atoms have the possibility of being scattered from the surface (Figure 3-1). [13]

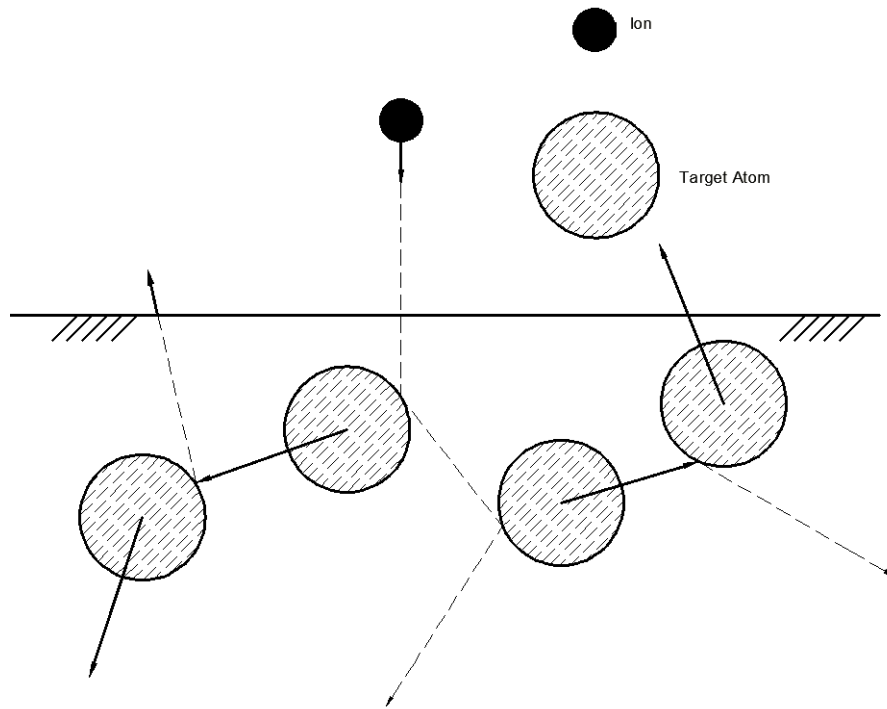


Figure 3-1: During sputtering an ionized particle collides with the target surface releasing target atoms. [13]

After a material has been vaporized, it can now be deposited. A suitable substrate is selected to grow a film of the sputtered material. The vaporized material condenses onto the substrate surface and forms a thin film.

3.1.1 Clusters

Often it is desirable to condense the vaporized, sputtered material before it reaches the substrate. This can create isolated clusters which allow for a greater control of the properties of the deposited material. Homogeneous nucleation of clusters results from increasing the distance between the target and the substrate, and decreasing the temperature within the chamber.

The sputtering process can create clusters of 10-2000 atoms. These clusters are of great interest in research because of their high surface-to-volume ratio. The growth of a material on a substrate does not necessarily guarantee growth in an equilibrium phase. Quenching from the vapor phase avoids nucleation and growth on the substrate surface. The deposited films are typically porous created from separation of the clusters. It is because of this porosity that the material can retain the high surface to volume ratio of the clusters [13].

Clusters can be reacted, mixed, or coated in situ to allow for greater possibilities for multi-component composites with nano-scale microstructures allowing for greater possibilities in material development. The significant advantage of these nanophase materials lies with the large volume fraction of atoms that occupy the grain boundaries. The small sizes and surface cleanliness, produced during deposition, allow restrictions in the phase equilibrium and kinetic equilibrium to be overcome during the synthesis. This results from the short diffusion distances, high driving forces and uncontaminated boundaries [13].

3.1.2 Cluster Process

Sputtering can be broken down into simpler steps consisting of the vaporization of a solid material, the nucleation and growth of the same material out of the vapor phase, and the deposition of that material onto a substrate. Initially an R.F. plasma is ignited in a mixture of argon and helium gases. The argon is used for bombardment of the target to vaporize the material, while the helium is used in the condensation of the vaporized material and for temperature stability. The plasma is kept close to the target by a magnetic field directly behind the target, known as magnetron sputtering (Figure 3-2). Large heating temperatures are possible during sputtering. For this reason, water jets are located behind the target to aid in cooling of the target material. [13]

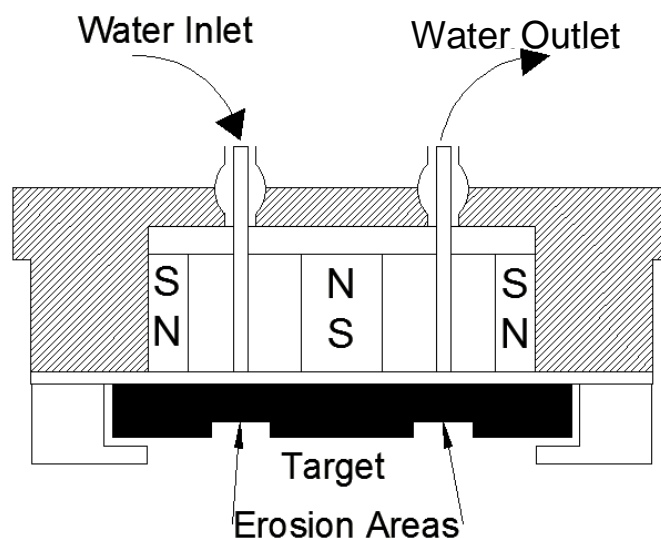


Figure 3-2: A magnetron sputtering device contains magnets located directly behind the target. The target is kept cool by a running water supply. [14]

The clusters nucleate and grow in size out of the vapor phase. The argon used during sputtering causes the initial nucleation of the clusters. Once the clusters attain a critical radius larger clusters grow from the seed clusters at a faster rate than new clusters can form. At this point, clusters develop from two-body, cluster-cluster collisions. Adjusting the flow rate of the helium in the sputtering chamber consequently will alter the size of the forming clusters. The nucleation and growth stage ends as the clusters exit the chamber through an expansion valve. The majority of clusters become ionized upon formation and thus can be focused and accelerated into an ionized cluster beam [13].

For experiments, it is desirable to preserve the size of the clusters upon deposition. It is possible to have high enough impact energy such that upon deposition the clusters will break apart. Therefore it is crucial that the impact energy be sufficiently low (1 eV per cluster atom) to avoid cluster breakage. The impact energy is directly proportional to the voltage supplied to the sample [15].

3.1.3 Sputtering Yields of Alloy Targets

The composition of the target, as well as its crystal structure is extremely important in the sputtering process. In the past, research has been done analyzing the crystal structure of the target and its role in the sputter deposition process. Many researchers have shown that the composition of the target is very close to the composition of deposited clusters. Temperatures of the target can become high enough to change the composition of the alloy target from thermal diffusion processes. The sputtering yield of the various elements of the alloy also plays a key role in the composition of the sputtered material [16].

Deposited layers of sputtered alloys show a tendency to change compositionally with the depth of the film. As a general rule the heavier component of the target always becomes enriched after sputtering. The reason for the preferred sputtering of these lighter elements is due to a closer match between the mass of the sputtering gas and the lighter atom. This mass similarity leads to a better energy transfer between atoms and thus yielding targets which have altered compositions and films with varying compositions [17].

3.1.4 Impact Dynamics

A major concern when depositing cluster materials is the result of the deposition onto a solid surface; upon collision with the surface there is a large redistribution of energy. Studies have shown that cluster implantation can occur at about 1 eV/atom [15]. According to C. Felix [18], an understanding of the landing process and the subsequent behavior of clusters during deposition is an essential first step. Currently there exists no method for organizing the clusters on the surface. Various methods have been proposed to try to attain cluster order such as, pinning the clusters to site defects or encapsulating them in organic molecules which are then dissolved following deposition are possible ways to obtain ordered arrays [18].

The deposition surface interrupts the cluster motion which in turn causes and can cause surface heating, structural deformation, fragmentation, splash evaporation of film atoms, the development of shock conditions and the dissipation of energy in the underlying crystalline substrate. These events are all possible when a nanocrystal with significant energy collides with a surface [19].

Difficulty in deposition comes from the individual energy of each atom. Upon deposition clusters penetrate into the surface, causing surface and structure irregularities. Clusters can also have significant energy to impact the surface and fragment creating smaller than desired clusters (Figure 3-3).

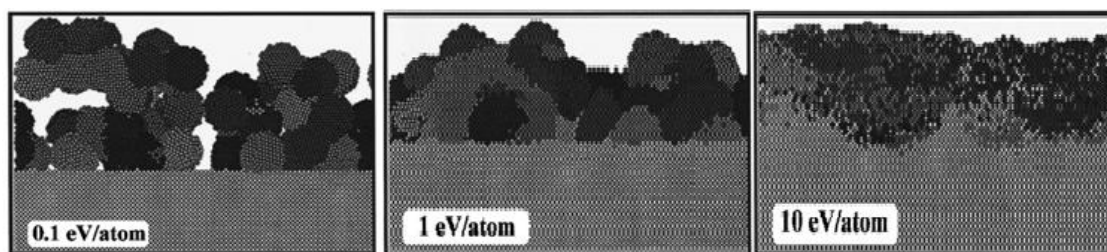


Figure 3-3: Deposition of clusters at various voltages. Clusters with low sputtering energy deposit on a substrate and retain their shape. Clusters with high sputtering voltages fragment and create thin films when deposited. [19]

This creates undesirable structures which will not have the high surface area to volume ratio. Deposition onto a buffer layer will act to dissipate the kinetic energy of the particle. Accelerating cluster with high initial energy followed by a low energy deposition was proposed in an article by Jensen; this would create a buffer layer to absorb energy from the impact [20]. In a series of experiments by Cheng [19], collisions were investigated on a rare-gas-fluid buffer layer finding that fragmentation, shock formation, and crater formation were all possible. With the use of a buffer layer these effects were drastically reduced. Although these collisions used a rare-gas-fluid buffer similar results are expected with other materials [19].

3.2 Mass Selector

The mass selector is capable of producing beams of well defined nanocrystalline particles through gas condensation methods. The size of the particles ranges from less than one nanometer to about 10 nanometers. The quadrupole mass analyzer filters the ions based on their mass-to-charge ratio. The four rods are placed in a parallel arrangement which allows for an ion path down the center of the rods. The rods only allow for ions of a certain mass-to-charge ratio to reach their target. Other ions have unstable trajectories which causes collisions with the rods (figure 3-5). Varying the applied voltage to the rods allows for precise selection of ion size. [21]

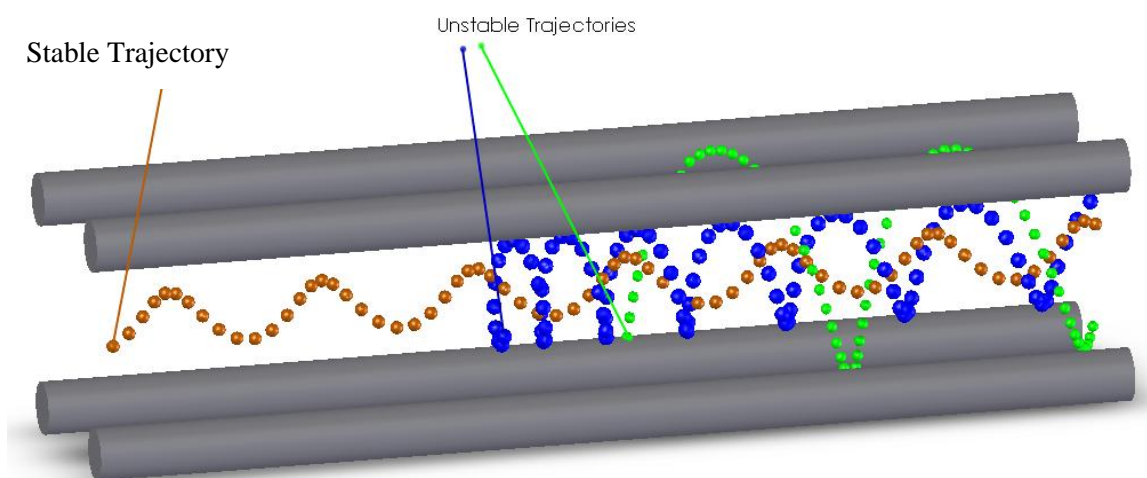


Figure 3-4: Diagram of quadrupole mass analyzer filtering ionized particles. Stable particle of desirable mass are accelerated through the device. Unstable particle of undesirable mass collide with the poles or are lost in the system. [22]

The mass selector can create an ionized beam which is accelerated toward the substrate to create a uniform coating. The mass selector is able to detect low mass clusters less than 200 amu and is specifically designed for the filtering of nanoclusters [22].

3.3 X-Ray Diffraction

X-ray diffraction is based on Bragg's law (Equation 3-1). Atoms arranged randomly scatter the x-rays in all directions; however atoms in periodic arrangement, such as crystals, directions which satisfy Bragg's law cause scattering and is known as diffraction. The amplitude

in diffraction is additive increasing the intensity at angles specific to the material. In directions which do not satisfy Bragg's law there is no scattering because the scattered x-rays cancel each other out [23].

$$n\lambda = 2d\sin\theta \quad (3-1)$$

The diffracted beam from a crystal is built up of rays scattered by the atoms in the crystal. The visible light reflection only takes place from the atoms located on the surface layer and will reflect at any angle of incidence. X-rays penetrate into the crystal lattice thereby giving knowledge of the crystal structure (Figure 3-5). Monochromatic x-rays only diffract at angles which satisfy Bragg's law which thereby create a diffraction pattern [23].

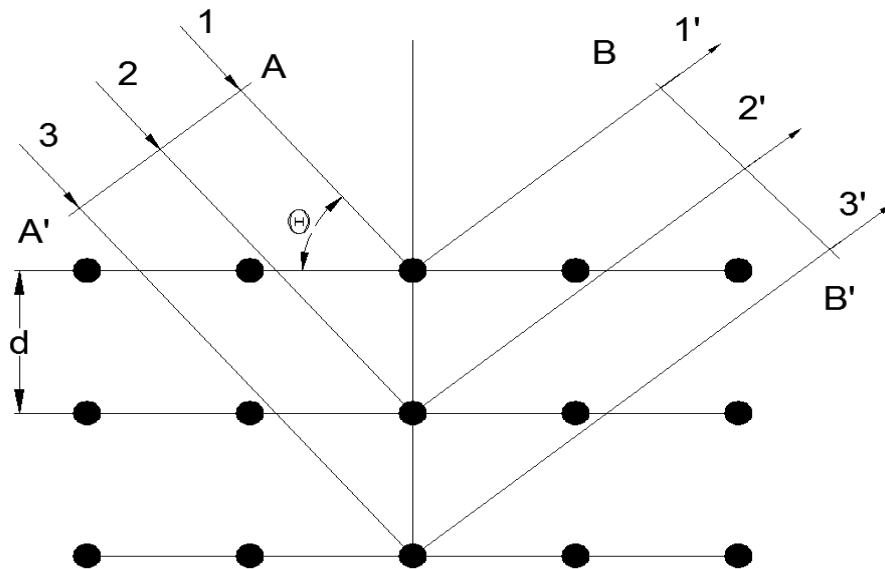


Figure 3-5: Diffraction of x-rays in a crystal lattice. X-rays will diffract off parallel planes according to Bragg's law. [23]

A single atom will scatter x-rays in all directions, however multiple atoms arranged in a periodic order will diffract at only Bragg angles. X-ray diffraction relies heavily on the crystallinity of a material. The diffraction pattern of solids is approximately zero everywhere except at Bragg angles. Liquids and amorphous solids tend to lack periodicity. These phases

tend to pack together in close arrangements and statistically show a preference for a certain interatomic distance. This results in x-rays that show one or two broad peaks [23].

3.4 Alternating Gradient Force Magnetometer

The alternating gradient force magnetometer (AGFM) is best suited for precisely measuring the magnetic properties of thin films and powders. The AGFM measures samples by utilizing a pair of field-gradient coils and a sensor element is made of two polarized sheets of metalized piezoelectric material cemented to the sample rod. The induced sample oscillates proportionally to its magnetization. The samples are mounted on a cantilever piezoelectric beam in order to attain more precise measurements; the opposite end of the piezoelectric element is rigidly clamped. The forces of the field gradient on the magnetized sample produce a bending moment on the element causing the vertically mounted sensor responds to horizontal forces. Specimens are attached using grease and positioned symmetrically at the center of the gradient field. The system is calibrated with a sample of nickel foil of known magnetic moment. The bending force generates a voltage proportional to the force on the sample to accurately measure of the hysteresis loops at various angles, both in-plane and out-of-plane anisotropy measurements. [24]

3.5 Transmission Electron Microscope

Transmission electron microscopes (TEM) produce images by transmitting an electron beam through a thin specimen. The image is then projected onto a screen, photographic film, or CCD camera for analysis. A TEM is capable of much higher resolutions than other microscopes.

Light microscopes lack the resolution to view specimens on the atomic level. The wavelength of light is much larger than a single atom which makes it impossible to view specimens at the atomic level under a light microscope. The TEM makes use of short-wavelength electrons which are sensitive to the atomic structure of materials.

3.5.1 Selected Area Diffraction

The diffraction patterns contain information about the crystal structure and lattice repeat distance, and the specimen shape. The primary electrons arriving at a material in the TEM interact with the atomic nuclei and atomic electrons in the material, causing the electrons to scatter [25].

The scattering of electrons creates constructive interference strongly at the Bragg angles and closely follows Bragg's law. Ring patterns are formed when the sample is polycrystalline. Indexing of these ring patterns is done in accordance with Bragg's equation [25].

3.5.2 Energy Dispersive Spectroscopy

The use of x-ray energy dispersive spectroscopy (EDS) is a valuable tool in materials research by giving a quantitative analysis of the material being examined. When inner shell electrons are ionized, an electron from the outer shell can fill in holes in inner shells. The energy difference from an electron moving from an outer shell to an inner shell is emitted in the form of an x-ray. Each material, when excited will give off a different unique x-ray characteristic of that material [25].

The detector first generates a charge pulse proportional to x-ray energy, which in turn creates hole-pairs in the semi-conductor. The number of electron hole-pairs is proportional to the x-ray photon energy. When a reverse bias is applied, electrons hole pairs separate and cause the electric pulses which are subsequently measured. The signal is then stored in channels assigned to the appropriate x-ray energy in a multichannel analyzer [25].

3.6 Superconducting Quantum Interference Device (SQUID)

For more accurate magnetic moment measurements the SQUID was used. The SQUID is capable of making sensitive measurements over a wide temperature range and is able to achieve

fields of several Tesla. The SQUID is housed in a magnetically isolated environment minimizing interference from the environment [26].

The SQUID uses a superconducting magnet to generate a field. The sample, placed within the field, is magnetized. The sample is then moved vertically through pick-up coils; the coils then measure the flux change. The signal is proportional to the magnetic moment of the sample [26].

4 Experimental Procedures

This section will discuss many of the procedures used during each test in detail. The specific details of the testing parameters are discussed as well as the various targets used. These experiments were performed using the gas condensation system belonging to Dr. David J. Sellmyer at the University of Nebraska-Lincoln. The system was constructed by Dr. Y. Qiang and Dr. Y.F.Xu. The system is equipped with one 3 in. DC magnetron sputtering source, one 2 in. DC magnetron sputtering source, and one 2 in. RF sputtering source (figure 4-1). The distance of the DC magnetron sputtering source, used in cluster creation can be adjusted to increase or decrease the length inside the chamber which directly affects the cluster growth. Samples were deposited on copper grids and capped with carbon to allow for imaging within the TEM.

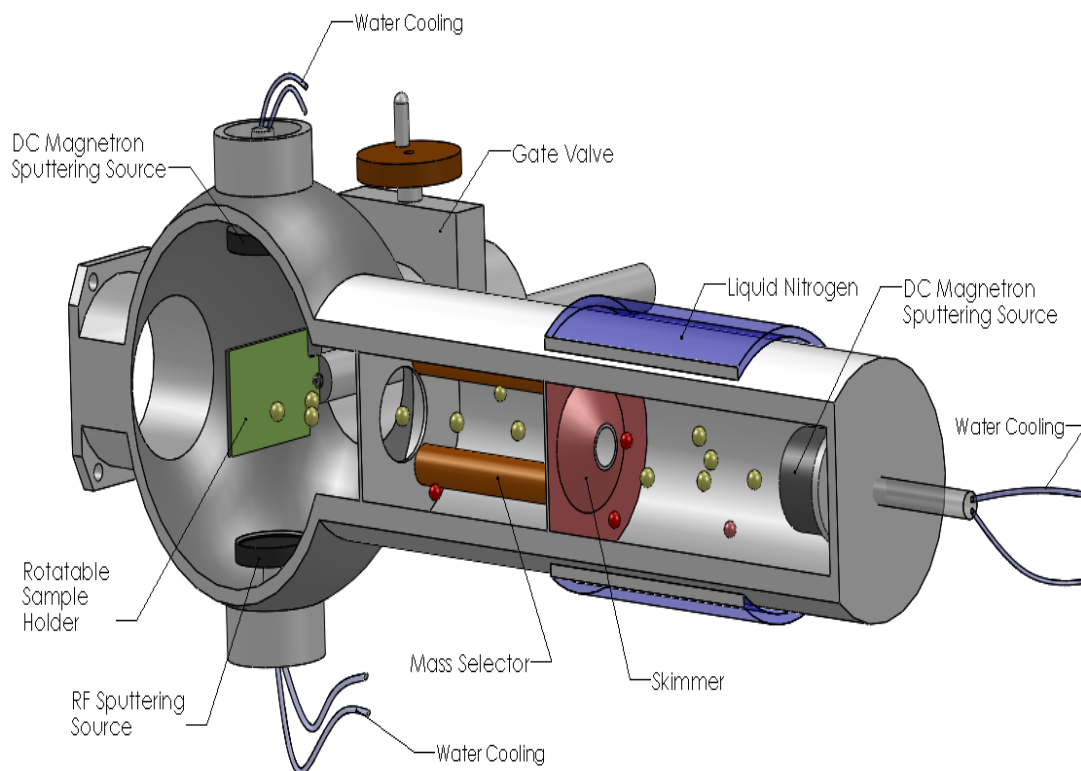


Figure 4-1: The cluster system at UNL. Clusters are created at the rightmost DC magnetron sputtering source and deposited onto substrates at the sample holder. The upper and lower sputtering sources can be used to create thin films on the sample.

4.1 $\text{Nd}_2\text{Fe}_{14}\text{B}$ Target

To create clusters of the correct composition a target of the correct composition had to be constructed. Three-eighths inch $\text{Nd}_2\text{Fe}_{14}\text{B}$ ingots were created by arc-melting, which resulted in negligible mass loss. These ingots were then cut into thin sections and inlaid in a three inch iron target (Figure 4-2) and were placed in a circular pattern in contact with one another. This pattern followed the race-track created during sputtering.

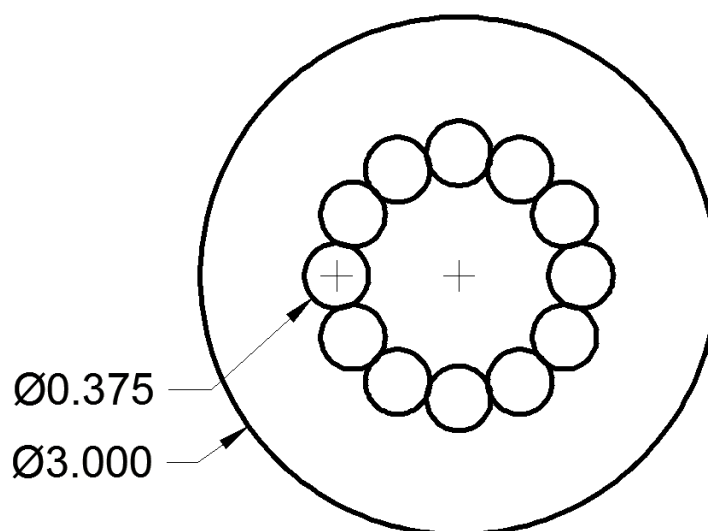


Figure 4-2: The composite sputtering target. The inner plugs of material follow the racetrack created during sputtering.

Clusters of a specific size were created with the use of a mass selector. Selecting the material density and acoustic impedance allows for an accurate selection of the cluster size. Adjustments were made to the Argon flow rate, Helium flow rate, and sputtering power to increase the deposition rate and to vary the sizes of the clusters created. Several TEM grids were also created to determine cluster size and composition.

Table 2: Experimental data from initial sputtering using the composite target

	1	2	3	4	5	6
Cluster Size (nm)	7.0-8.6	6.7-8.91	7.01-8.32	5.11-6.72	5.31-6.97	7.21-8.58
Ar Flow Rate	300	250	320	270	320	251
He Flow Rate	125	95	100	126	100	59
Deposition Rate (Å/sec)	0.3	0.3	0.4	0.4	0.4	0.4
Cap Layer	Carbon	Carbon	Carbon	Carbon	Carbon	Carbon
Temperature (°C)	-127	-127	-127	-132	-132	-131
Thickness (nm)	30	30	30	30	30	30
Special Notes	None	None	None	None	None	1 nm Carbon Layers 2 nm Cluster Layers

4.2 Cluster Deposition using a (Fe-Co)-Nd-B Target

The target used was a 2 in. target used in the creation of thin films. A modified holder was created to allow the target to be used on the 3 in. sputtering gun. Because of a problem with the mass selector, clusters of varying size were created.

Table 3: Sputtering parameters used for the (Fe-Co).Nd-B target

	1	2	3	4	5	6
Cluster Size (nm)	N.A.	N.A.	N.A.	N.A.	N.A.	N.A.
Ar Flow Rate	300	300	300	300	300	300
He Flow Rate	100	100	100	100	100	100
Deposition Rate (Å/sec)	0.6	0.6	0.6	0.5	0.7	0.7
Cap Layer	1 nm Carbon	1 nm Carbon	1 nm Carbon	1 nm Carbon	1 nm Carbon	1 nm Carbon
Temperature (°C)	-131	-131	-131	-131	-131	-131
Thickness (nm)	30	30	30	30	45	60
Power (W)	49	49	49	43	49	49

5 Results and Discussion

5.1 As Deposited Clusters

Examination of the composite target showed an irregular racetrack had been created during sputtering. In a number of areas material had been sputtered from the iron plate rather than the $\text{Nd}_2\text{Fe}_{14}\text{B}$ plugs. Comparing the coverage area of the racetrack on both the $\text{Nd}_2\text{Fe}_{14}\text{B}$ plugs and the iron plate showed an excess of approximately 7% iron was sputtered during deposition.

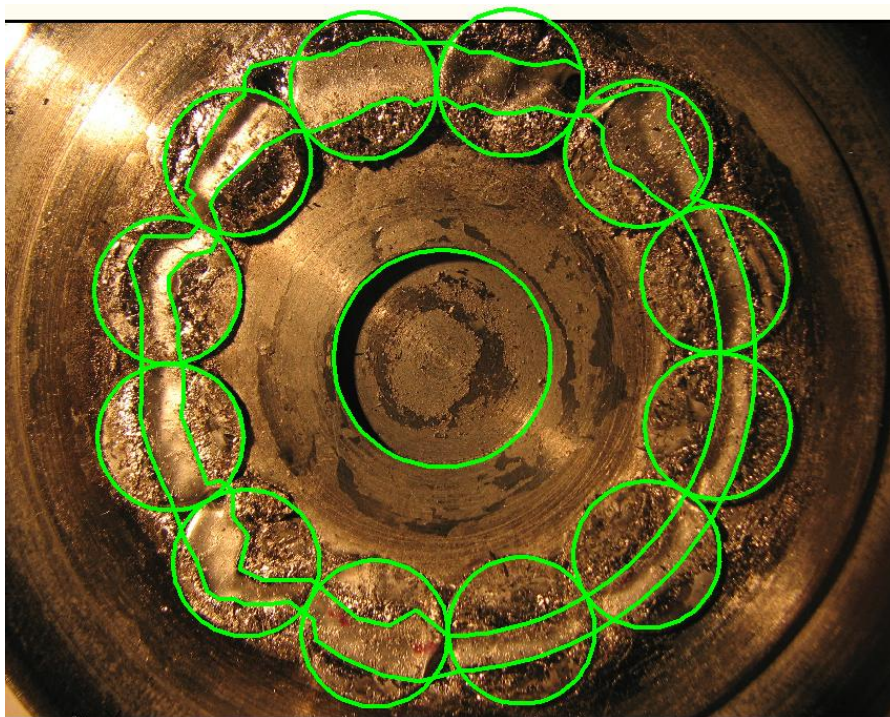


Figure 5-1: Composite target used during deposition. The racetrack as well as the plugs has been outlined.

TEM examination confirmed that the clusters were approximately 8nm in size (Figure 5-2). Determining the composition of the clusters proved difficult due to the small volume of material contained on the TEM grid.

The TEM images provided information about the size and shape of the clusters created. In general the clusters were circular in shape with few irregularities. There was no evidence of cluster fragmentation upon deposition. In each image the maximum diameter of the clusters was measured.

The clusters were amorphous upon deposition. This is evident from the diffraction patterns obtained from the samples. As seen in the diffraction pattern in Figure 5-2 there are diffuse rings present in the diffraction pattern. These rings would appear much sharper if the material was crystalline.

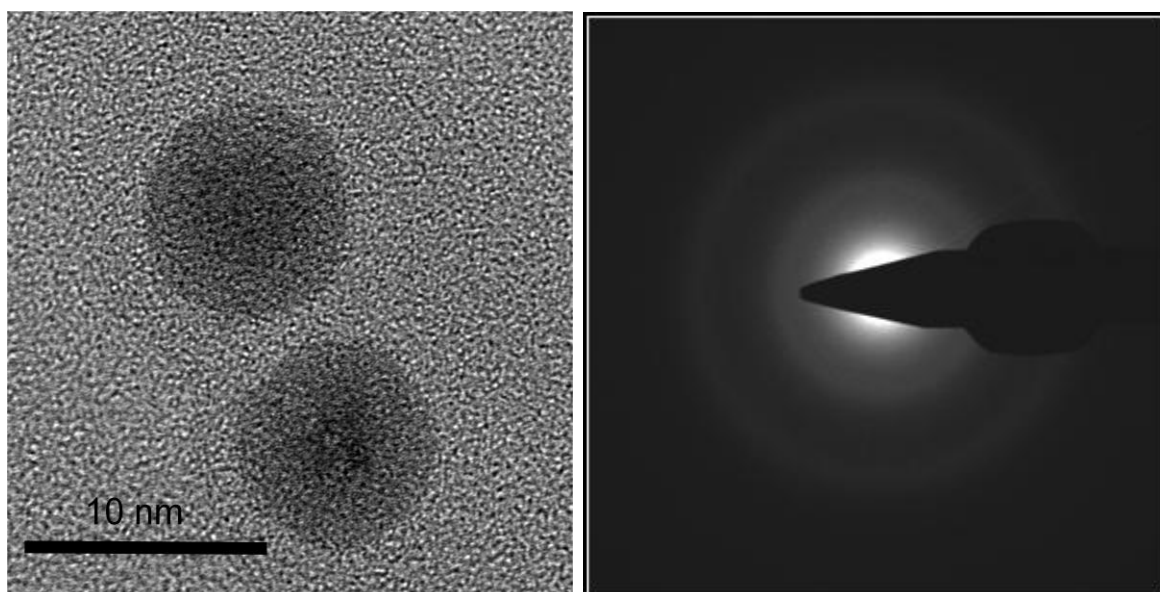


Figure 5-2: As-deposited clusters with an average diameter of 8.1 nm (left) as seen from bright field TEM. The diffraction pattern (right) from the clusters shows diffuse rings indicating amorphous structures.

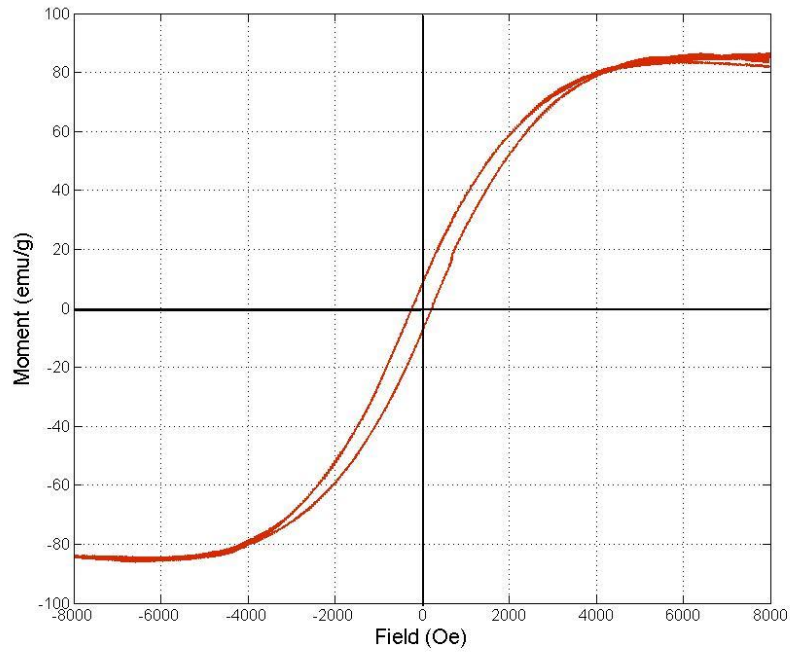


Figure 5-3: The AGFM data of as-deposited clusters from the composite target.

The clusters had poor magnetic properties (as seen in figure 5-3) when compared to that of bulk $\text{Nd}_2\text{Fe}_{14}\text{B}$. The irregular racetrack pattern on the sputtering target combined with the soft magnetic properties of the as-deposited clusters, and the low coercivity post-annealing all lead to the conclusion that the wrong composition of clusters had been deposited. For these reasons an alloy target of $\text{Nd}-(\text{Fe-Co})-\text{B}$ was used to make additional clusters.

The images from the TEM provided accurate information on the actual amount of material that had been deposited. Using the TEM images, the number of clusters in each image along with the diameter of each was measured. From these measurements an estimated volume of the clusters was calculated. Using this actual volume compared to the expected volume during deposition of the TEM samples, a ratio was established to predict the amount of material deposited on the silicon substrates equation (5-1). This gave an accurate measurement of the mass of material deposited.

$$\frac{V_{TEM \text{ actual}}}{V_{TEM \text{ expected}}} = \frac{V_{Si \text{ actual}}}{V_{Si \text{ expected}}} \quad (5-1)$$

A series of bright field images were taken with the use of the TEM. This provided a number of images to obtain an accurate description of the particle diameters during sputtering. Of these images five taken from the same magnification from various areas of the TEM grid provided the maximum diameter of approximately 120 clusters. Clusters which fell on the boundary of the images were excluded from analysis since a maximum diameter could not be determined from the incomplete image of these clusters.

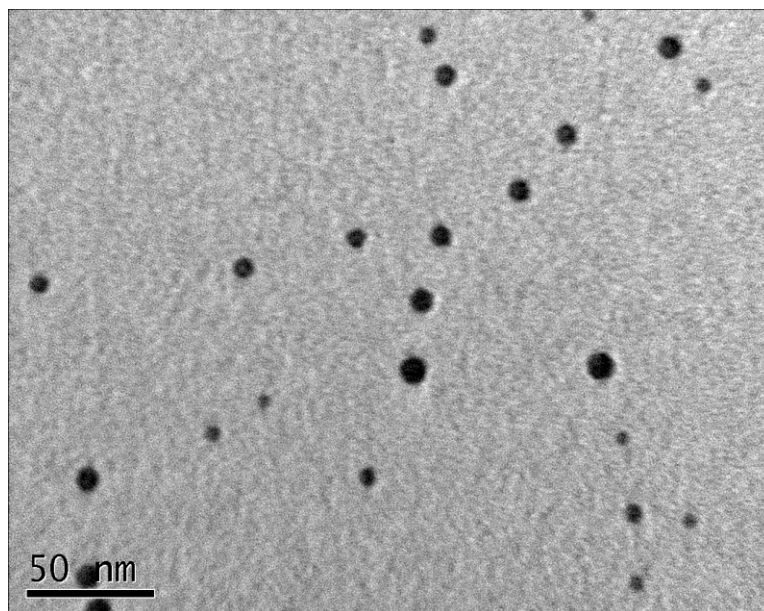


Figure 5-4: TEM image of as-deposited clusters used for size analysis.

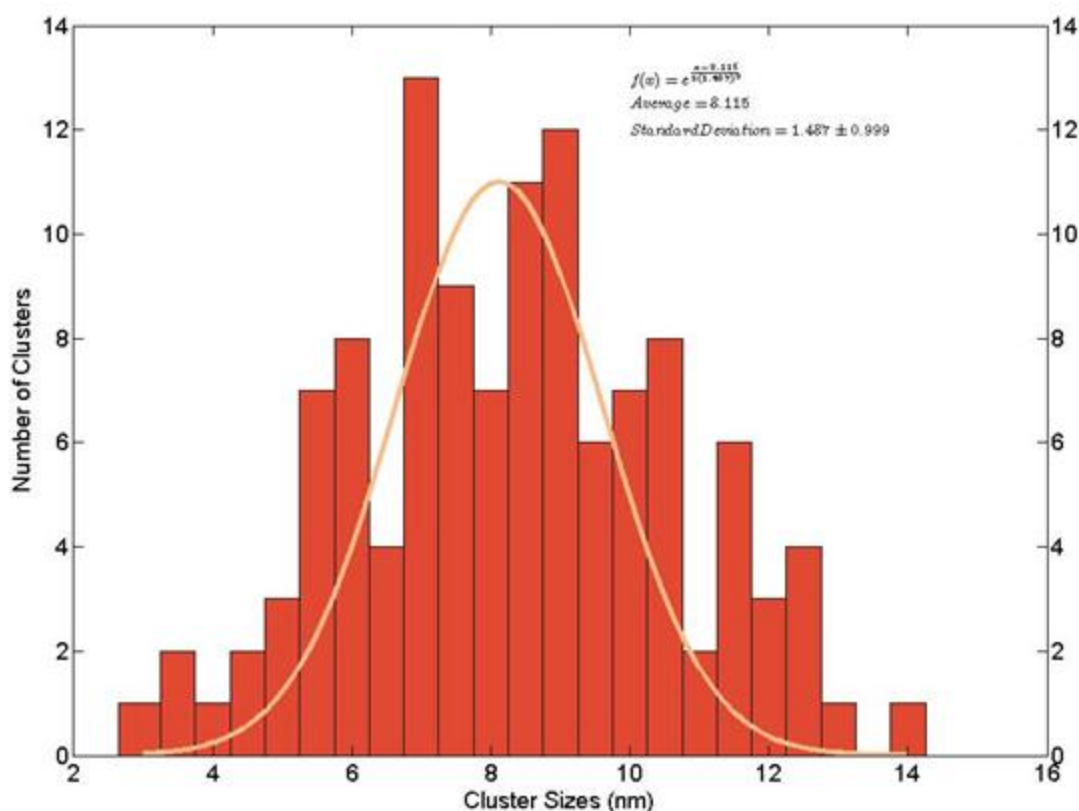


Figure 5-5: The distribution of cluster sizes from five TEM bright field images

Clusters were then deposited to create a thin layer of material for analysis in SQUID and EDS. This provided a suitable amount of material for analysis. Enough clusters were deposited to create a solid layer of material. The clusters were also amorphous as seen in Figure 5-6 from the diffuse rings observed in the diffraction pattern.

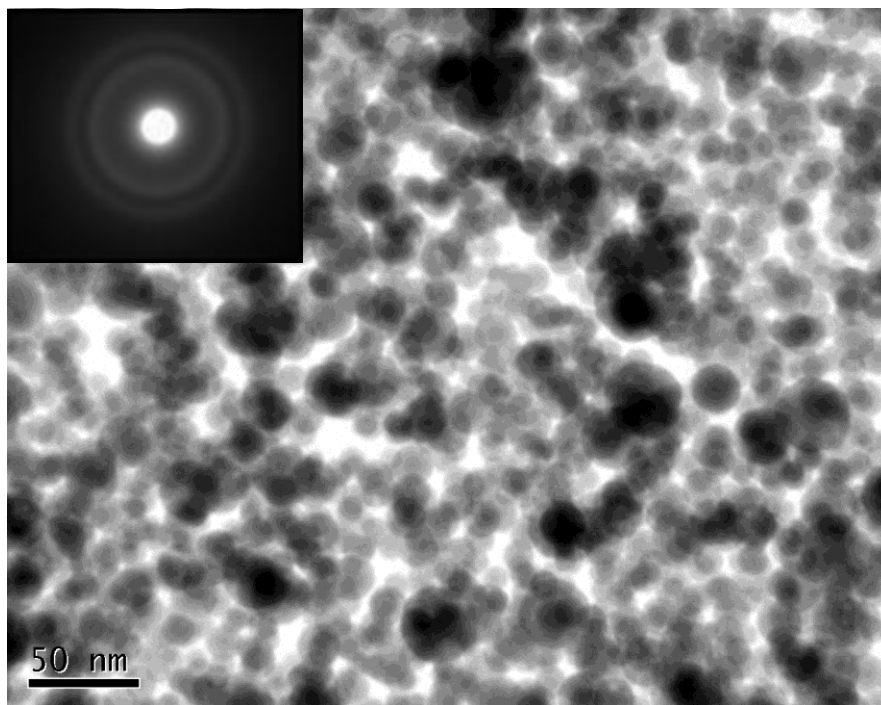


Figure 5-6: A film of as-deposited amorphous clusters approximately 15nm thick. The diffraction pattern (inset) shows diffuse rings confirming clusters are amorphous.

The EDS proved to be very useful in the course of analysis. EDS data from multiple areas were acquired. Within experimental error, compositions were the same in each area (Figure 5-5, Table 4).

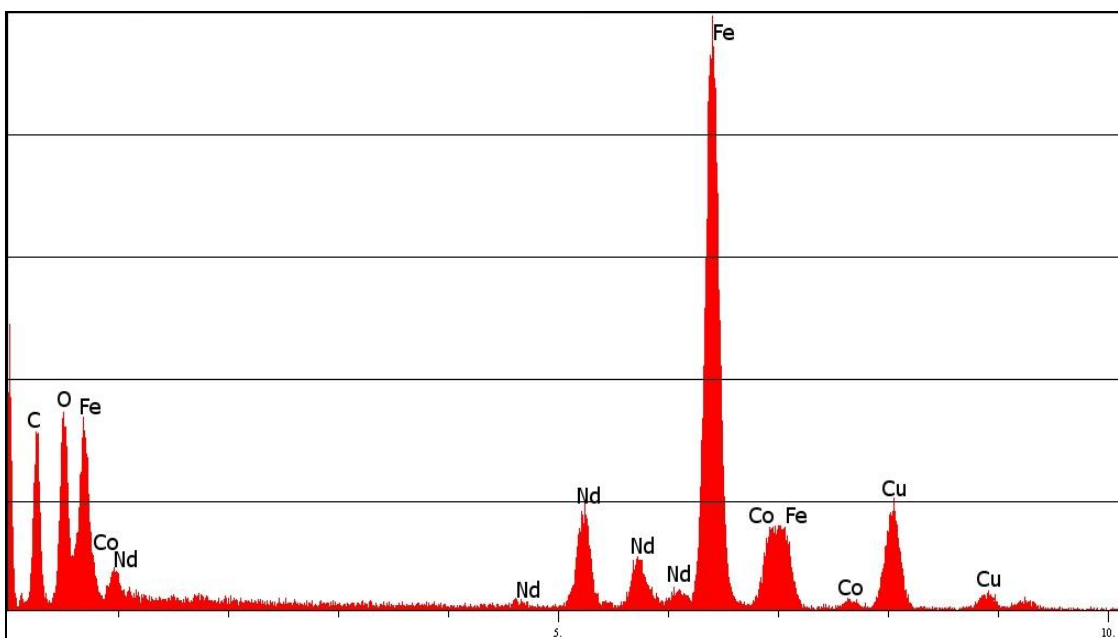


Figure 5-7: EDS spectrum of cluster material. Copper is present from the TEM grid. Carbon was used to cap the clusters. Oxygen indicates some of the sample has become oxidized.

Boron is difficult to detect with EDS because of low-energy x-ray absorption by the window in front of the detector. Carbon is present in the spectrum from the carbon coating deposited on samples after deposition to prevent oxidation. Although great care was taken in all steps of sample preparation to prevent oxidation, it is unavoidable. There is also a minor peak for copper from the copper grid onto which the clusters were deposited.

Table 4: The EDS data from the clusters material and the bulk target.

Element	Atomic Percent	
	As Deposited	Bulk Target Material
Fe	79.068	79.297
Co	8.107	6.673
Nd	12.825	14.03

The composition of the clusters was compared to that of the target material. The analysis of the target also provided useful insight into the clusters. The target material was examined in the SEM using the EDS. The EDS spectrum of the target material qualitatively showed the same composition of the target material and deposited clusters. The sample area of the SEM is larger

than that of the TEM, this and the relatively weak signal from the TEM can explain the quantitative differences seen between the clusters and the target. The composition of the clusters appears to be stoichiometrically similar to the target. Comparing the ratio of transition metals to rare-earth metals in both the target and the clusters shows a strong correlation between the cluster material and the target composition.

An EDS analysis was also performed within the racetracks of the target material. However, due to the geometry of the racetracks the EDS analysis lacks accuracy and is therefore not included in the analysis.

Magnetic Behavior

Two different samples, annealed and as-deposited, were tested using the SQUID. Both samples were deposited on silicon substrates with masses calculated using the formula in equation (5-1). Hysteresis loops were measured for each sample at 300 K and 10 K. A high field was used so the diamagnetic signal of the silicon would become clear. By measuring the slope of the diamagnetic signal a correction factor for the loop could be calculated and applied.

Superparamagnetism is exhibited in material with very small crystallites (1-10 nm). The temperature effects at room temperature are sufficient enough to overcome the coupling effects between each of the particles. Therefore, at room temperature, there is no longer any magnetic order and the internal magnetic field no longer exists causing paramagnetic behavior. When the temperature is not sufficient enough to overcome the coupling forces in the particles instead of each individual particle being influenced by an external magnetic field, the entire crystallite aligns with the magnetic field [27].

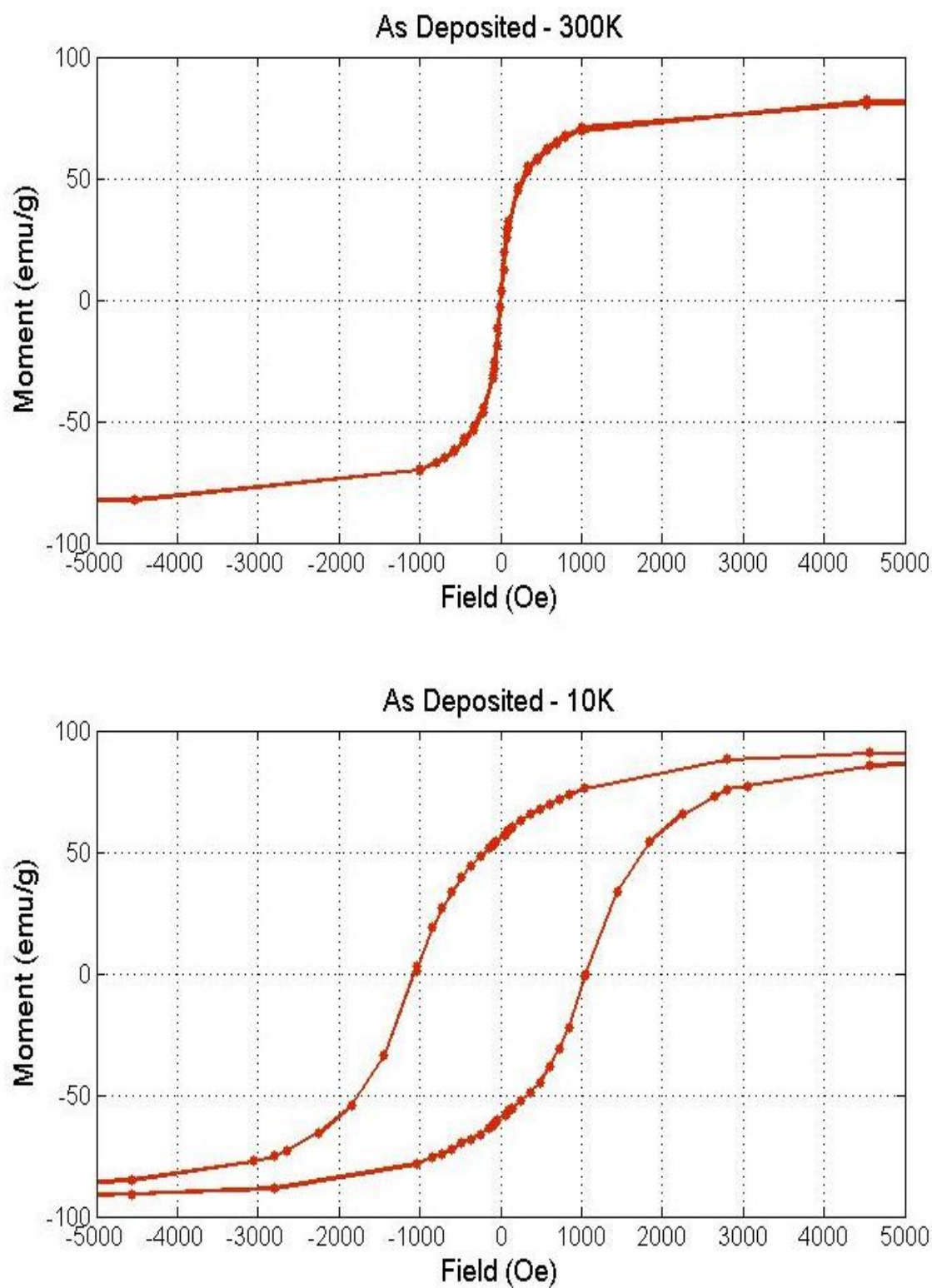


Figure 5-8: The SQUID analysis of as-deposited cluster material at 300 K (upper graph) and 0 K (lower graph) shows superparamagnetic properties at high temperatures and ferromagnetic properties at low temperatures.

5.2 Annealing

Since the as-deposited clusters were amorphous, annealing studies were conducted to crystallize the clusters, and then the crystallization products were determined.

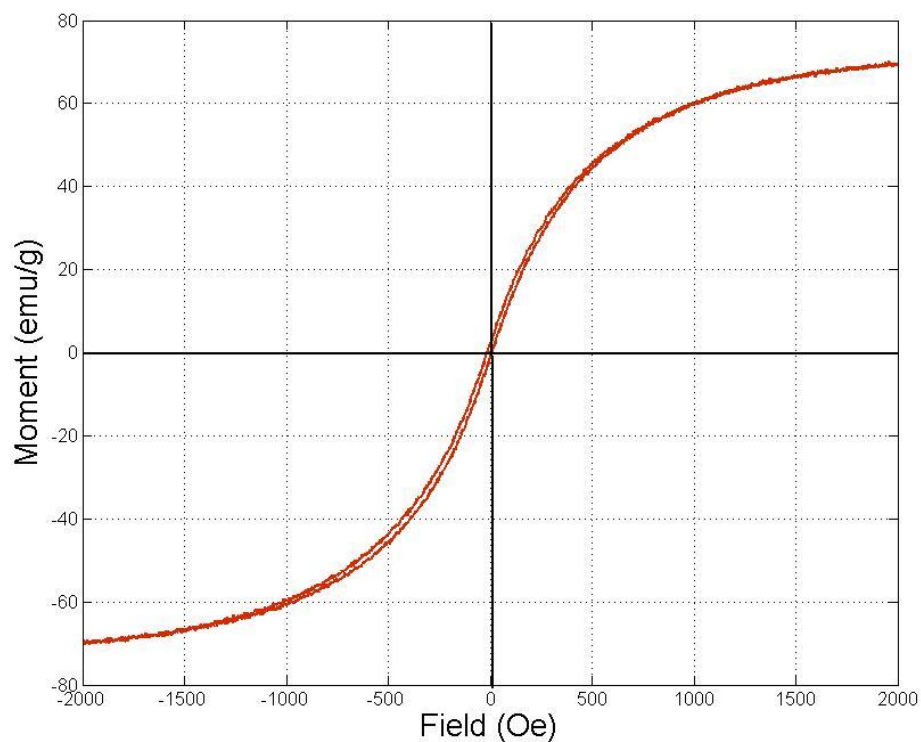


Figure 5-9: AGFM data of the as-deposited cluster material. The hysteresis loop shows a soft-magnetic material.

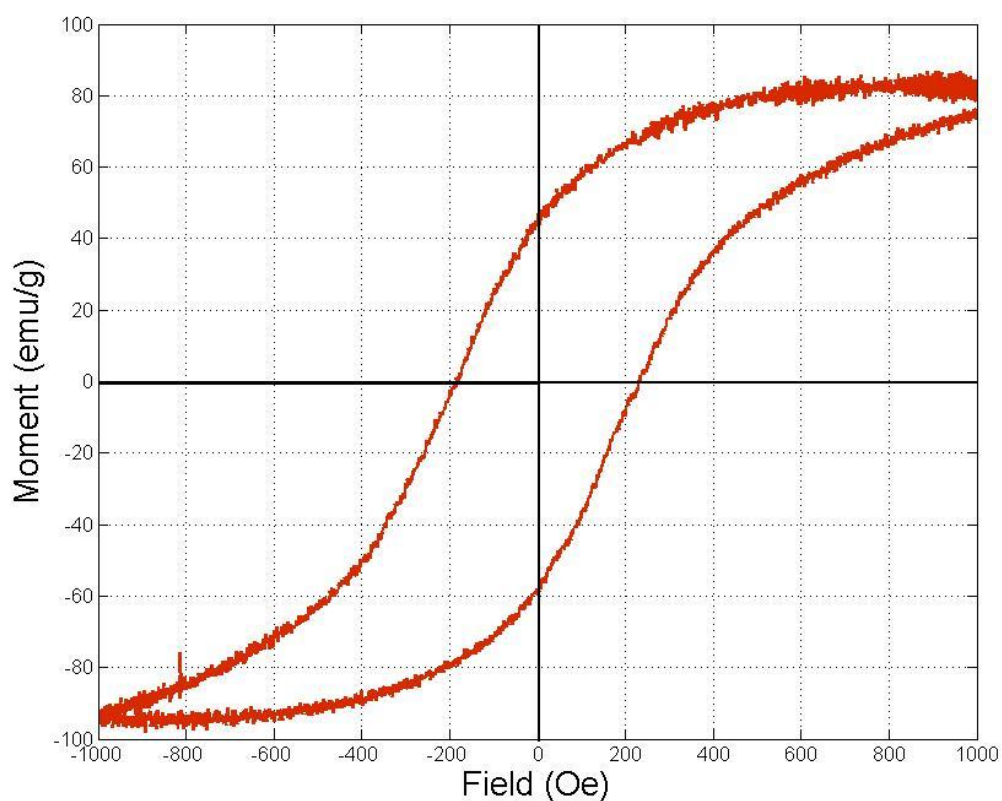


Figure 5-10: AGFM data of annealed cluster material. The clusters were annealed for four minutes at 600°C.

Annealing the as-deposited cluster material does cause sintering of the individual clusters, in essence creating a thin film. Normally the clusters would be kept isolated during annealing; however the primary goal here was to understand the crystallization products. This reveals the overall composition of the clusters with respect to B content, assuming equilibrium is achieved.

Annealing has in the past been done on $\text{Nd}_2\text{Fe}_{14}\text{B}$ with two underlying assumptions as to the increase of coercivity. Samples were annealed in a rapid thermal annealing device for various time intervals after being flushed with argon for 15 minutes. Annealed samples showed an initial increase in coercivity, but lacked further increases with subsequent annealing.

The magnetic properties of deposited clusters were tested using the AGFM. Samples were annealed in an inert argon-gas atmosphere at 600°C. The coercivity was determined at various intervals during this process. Results show the material deposited had poor magnetic properties. This likely indicates a material other than $\text{Nd}_2\text{Fe}_{14}\text{B}$ has been deposited.

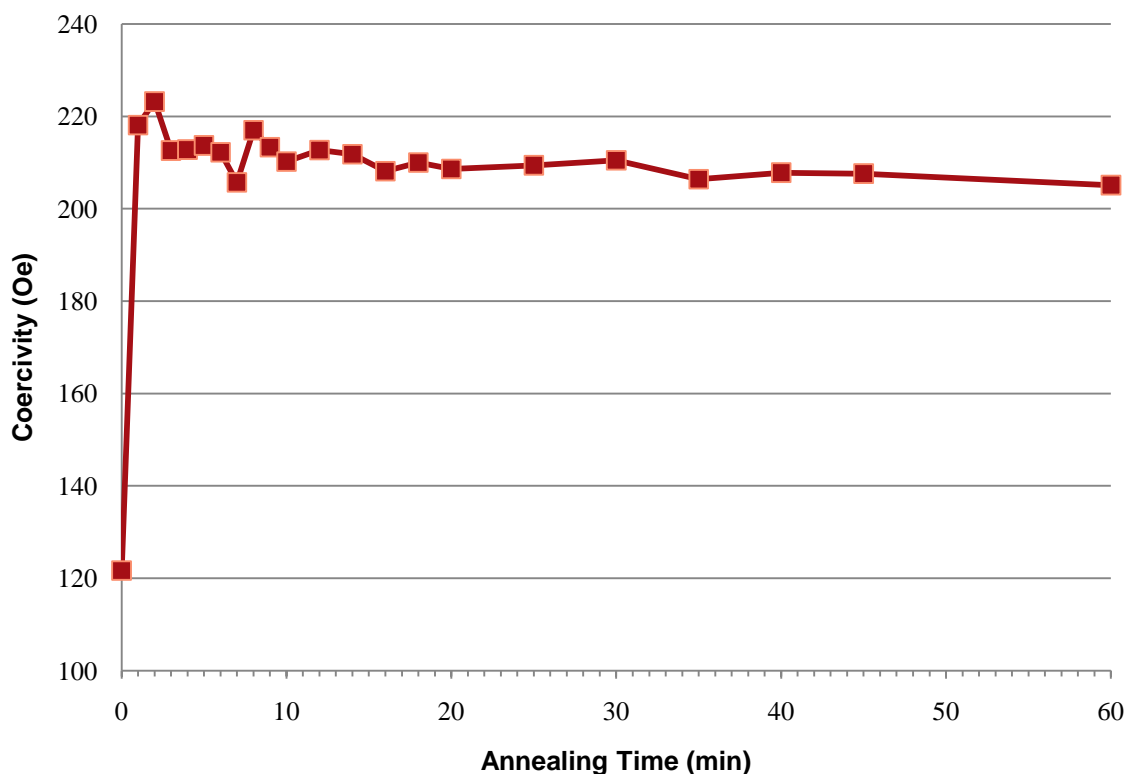


Figure 5-11: The dependence of coercivity as a result of annealing time. Samples were annealed at 600°C in an inert gas atmosphere.

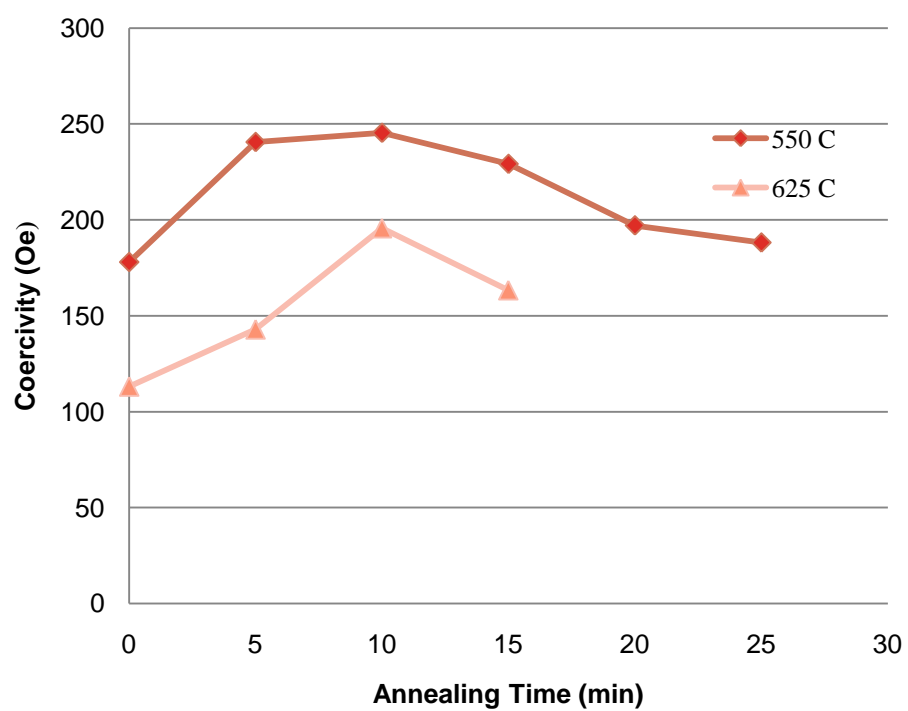


Figure 5-12: The dependence of coercivity at different annealing temperatures with increasing time.

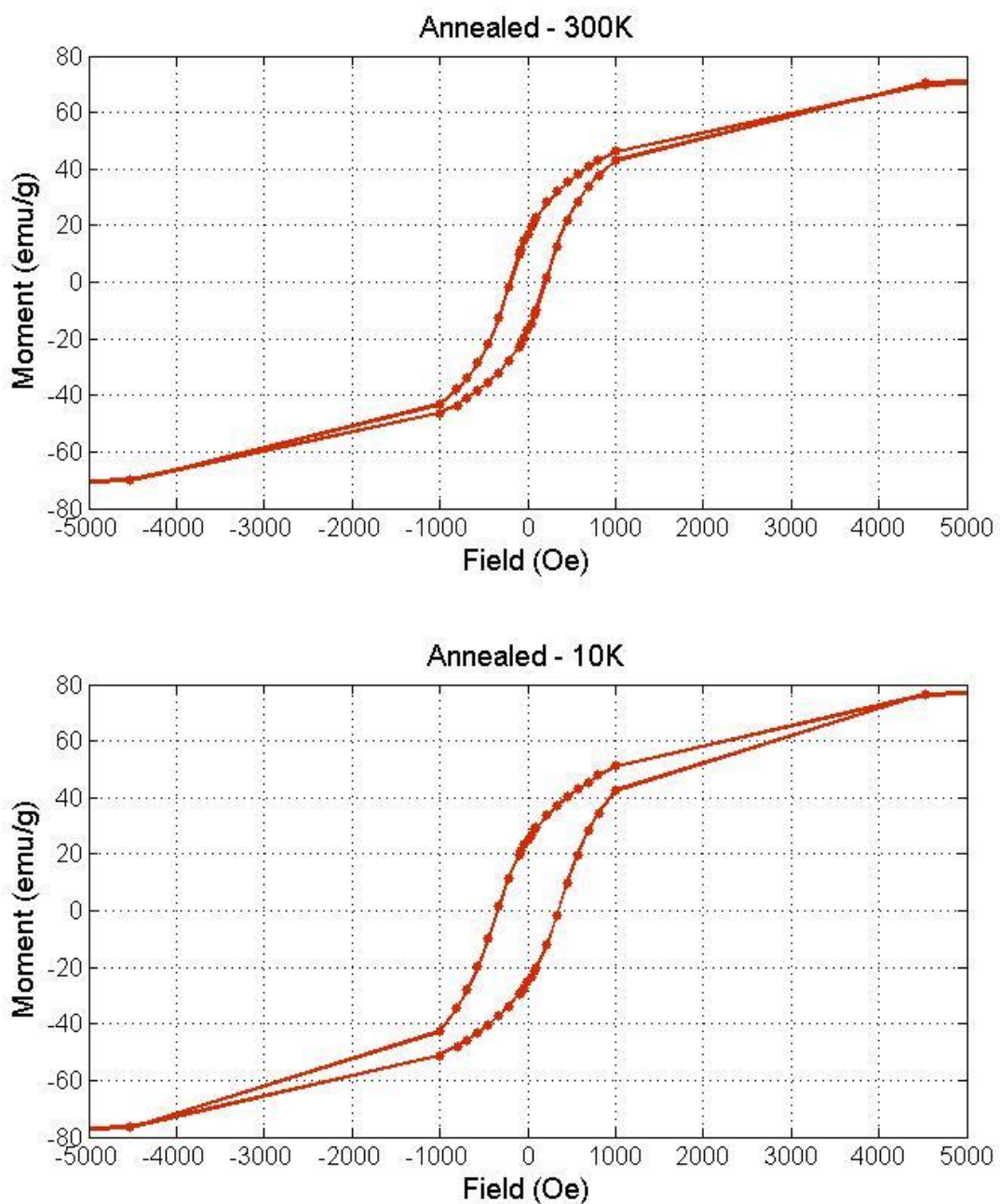


Figure 5-13: The SQUID analysis of annealed cluster material at 300 K (upper graph) and 0 K (lower graph). There is a moderate increase in coercivity at low temperatures.

Transmission electron microscopy was utilized to analyze the structure of the clusters.

As seen in Figure 5-14 of the annealed cluster film, the contrast suggests that the clusters are crystalline, which was confirmed by SAD (insert in Figure 5-6).

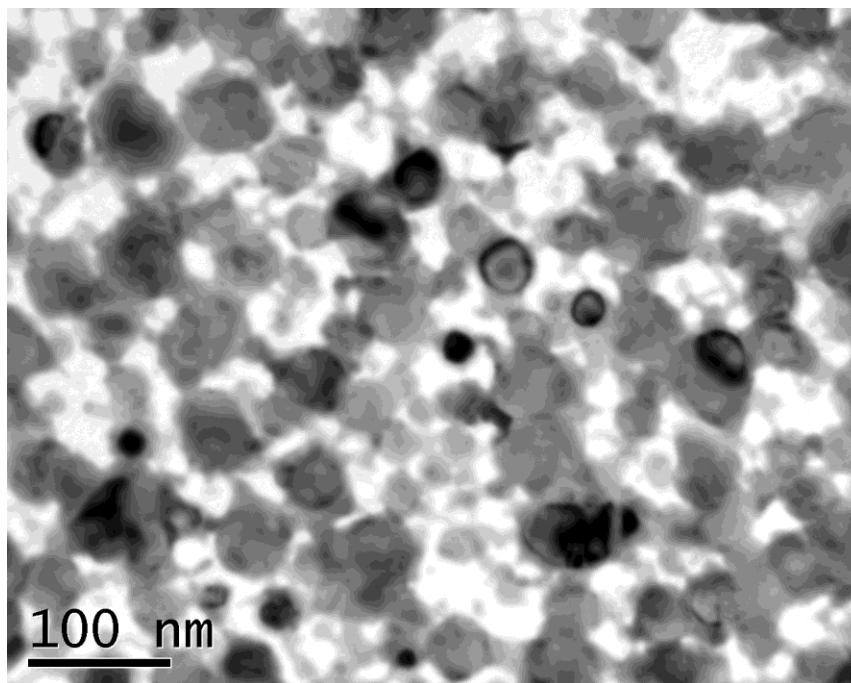


Figure 5-14: TEM image of a thin film of annealed clusters approximately 15 nm thick. Sintering has occurred between cluster particles.

The EDS analysis of the annealed clusters showed a similar composition as the as-deposited clusters. This indicates there were minimal compositional changes from annealing in the cluster material.

Table 5: The EDS data taken from the cluster material compared to the target material

Element	Atomic Percent	
	Annealed	Bulk Target Material
Fe	79.431	79.297
Co	8.048	6.673
Nd	12.521	14.03

Selected area diffraction techniques were performed on annealed samples to obtain patterns which would provide information on crystal structure. The diffraction pattern of the annealed samples revealed crystalline samples.

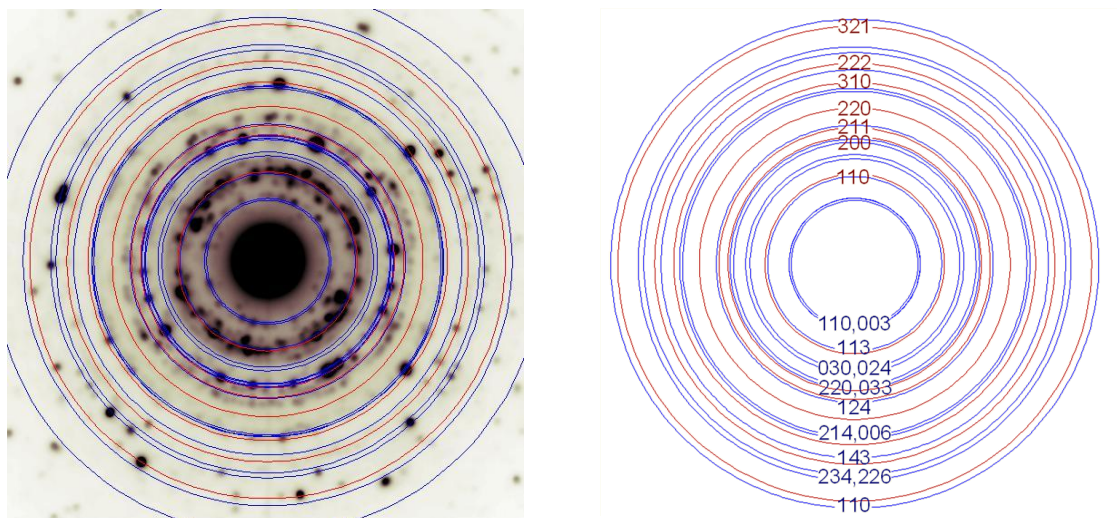


Figure 5-15: Indexed SAD patterns of cluster samples. The bcc-Nd is shown in red and $\text{Nd}_2\text{Fe}_{17}$ is shown in blue.

The diffraction pattern was compared to standards for possible phases in the Nd-Fe-B system. Since the initial target was close to the $\text{Nd}_2\text{Fe}(\text{Co})_{14}\text{B}$ stoichiometry, the 2-14-1 structure was initially assumed. However, the diffraction rings did not match with this structure. The search was then broadened to phases near $\text{Nd}_2\text{Fe}_{14}\text{B}$, including NdB_4 , FeB , Nd_2B , $\text{Nd}_{1.1}\text{Fe}_4\text{B}_4$, γFe , $\text{Nd}_2\text{Fe}_5\text{B}_5$, and $\text{Nd}_2\text{Fe}_{17}$. The $\text{Nd}_2\text{Fe}_{17}$ appeared similar to the diffraction pattern; however major peaks in the diffraction pattern were unaccounted for. Oxides of neodymium and iron were considered in case oxidation had occurred. Since there is an affinity for elements of lower atomic mass to be quickly depleted during the sputtering process the phases of the Nd-Fe system were then considered figure 2-14.

From the diffraction patterns the TEM samples contain both $\text{Nd}_2\text{Fe}_{17}$ and a bcc-Nd phase. From the phase diagrams (Figure 2-13) this is indicative of a loss of boron during the sputtering process. Stable phases in the Nd-Fe-B were all considered during examination of the phase diagrams.

The diffraction patterns show a strong presence of bcc-Nd. Metallic Nd has a double-hexagonal cubic packed structure at temperatures below 863°C and forms the β -Nd (bcc) structure at higher temperatures. The face-centered-cubic phase does not appear in Nd. There are three possible crystal structures for the oxides of Nd, hexagonal, monoclinic, and cubic. However the later two structures are metastable structures. [28]

It is not uncommon to produce metastable structures during thin film deposition, however these structures tend to transform to stable structures during annealing. In ultra-thin films there are large departures from the lattice constants, which vary with the surface energy. This may be caused by deposition conditions or from the influence of the substrate. [16]

Grain boundaries of $\text{Nd}_2\text{Fe}_{14}\text{B}$ consist of approximately 90% Nd [28]. The Nd grain boundaries are found to be amorphous in $\text{Nd}_2\text{Fe}_{14}\text{B}$. The Nd boundary phase has been studied extensively by Tsubokawa et al. Neodymium has a tendency to form the bcc boundary phase, along surface interfaces when oxidized at an elevated temperature [29]. Considering the large surface area available in the cluster films this phase could be easily formed.

The magnetic properties of the as-deposited material were tested using the SQUID. The as-deposited sample exhibited superparamagnetic properties at room temperature and ferromagnetic properties at low temperatures. The SQUID data revealed poor magnetic properties of the samples, but was in agreement with reported saturation magnetism for $\text{Nd}_2\text{Fe}_{17}$ of 90.9 emu/g [30].

6 Conclusions

Clusters of uniform size and shape were created with the gas condensation system. TEM analysis showed clusters were amorphous upon deposition and had an average size of 8nm. In order to create clusters from a Nd-Fe-B target a moderate sputtering power of approximately 50 watts needs to be used as well as relatively high flow rates of both argon and helium.

Clusters were created were two-phase $\text{Nd}_2\text{Fe}_{17}$ and bcc-Nd; the bcc-Nd phase is stabilized by oxygen during the annealing process. Cluster composition was deficient in boron, which is likely lost during the sputtering process. To remedy, this boron should be added in subsequent tests.

Magnetic properties of the clusters were similar to the properties of $\text{Nd}_2\text{Fe}_{17}$. Although annealing increased the coercivity of the deposited clusters at room temperature, this ultimately lead to a deterioration of properties at lower temperatures. The as-deposited samples became ferromagnetic at low temperatures and exhibited superparamagnetic properties at room temperature. These properties are indicative of amorphous rare-earth transition metal clusters. The addition of boron to the sputtering target should increase the coercivity and energy product of the samples.

In order to obtain $\text{Nd}_2\text{Fe}_{14}\text{B}$ clusters, future work should be carried out with additional boron to the target. Calculating the boron present in the target and adding chips to the target should produce clusters which are stoichiometrically correct.

7 Works Cited

1. Cohen, Morris, [ed.]. *Introduction to Magnetic Materials*. Reading, Massachusetts : Addison-Wesley Publishing Company, 1972. pp. 181-202, 287-351, 556-626. Vol. 11.
2. Rui, X. and Shield, J. E. In-Cluster-Structured Exchange-Coupled Magnets with High Energy Densities. 2006, Vol. 89, 122509.
3. Callister, William D. *Materials Science and Engineering an Introduction*. New York : Von Hoffman Press, 2002. pp. 673-700. Vol. 11.
4. Tebbel, R. S. *Magnetic Domains*. Great Britain : Methuen & Co LTD, 1969.
5. Weng, Robert S., WIJ, Jiin-Chuan and Kryder, Mark H. The effect of random coercivity on domain growth processes in rare earth-transition metal alloys. 1991, Vol. 69, 8, pp. 4856 - 4856.
6. Berkowitz, Ami E. and Kneller, Eckart. *Magnetism and Metallurgy*. New York : Academic Press, Inc., 1969.
7. Skomski, Ralph and Coey, J.M.D. *Permanent Magnetism*. Philadelphia : Institute of Physics Publishing, 1999.
8. Raghavan, V. B-Fe-Nd (Boron-Iron_Neodymium). 2003, Vol. 24, 5.
9. Zhang, W., Liu, G. and Han, K. Fe-Nd (Iron-Neodymium). [book auth.] Thaddeus B. Massalski. *Binary Alloy Phase Diagrams*. ASM International, 1990.
10. Parhofer, S., et al. Magnetic Properties and Growth Texture of High-Coercive Nd-Fe-B Thin Films. 1998, Vol. 83, pp. 2735-2741.
11. Castaldi, L., Davies, H. A. and Gibbs, M. R. J. Growth and Characterization of NdFeB Thin Films. 2002, pp. 242-245.
12. *Magnetic Properties and Magnetic Domains of Nd-Fe-B Thin Films*. S. L. Chen, W. Liu, Z. D. Zhang, and G. H. Gunaratne. 2008, Journal of Applied Physics.
13. Sigmund, Peter. Theory of Sputtering. I. Sputtering Yield of Amorphous and Polycrystalline Targets. 1969, pp. 383-415.
14. Chapman, Brian. *Glow Discharge Processes*. New York : John Wiley & Sons, 1980.
15. Abbet, Stephane, et al. Synthesis of Monodispersed Model Catalysts Using Softlanding Cluster Deposition. 2002, pp. 1527-1535.
16. Wasa, Kiyotaka and Hayakawa, Shigeru. *Handbook of sputter deposition technology: principles, technology, and applications*. Park Ridge : Noyes, 1991.

17. Liao, Z. L. Surface-layer composition changes in sputtered alloys and compounds. June 15, 1977, Vol. 30, 12, pp. 626-628.
18. Felix, C. and Vandoni, G. Morphology and Evolution of Size-Selected Metallic Clusters Deposited on a Metal Surface. 1998, Vol. 57, 7, pp. 4048-4052.
19. Cheng, Hai-Ping and Landman, Uzi. Controlled Deposition, Soft Landing, and Glass Formation in Nanocluster-Surface Collisions. 1993, pp. 1304-1307.
20. Jensen, Pablo. Growth of Nanostructures by Cluster Deposition: Experiments and Simple Models. 1999, Vol. 71, 5, pp. 1695-1735.
21. de Hoffmann, Edmond and Stroobant, Vincent. *Mass Spectrometry: Principles and Applications*. Toronto : John Wiley & Sons, 2003. p. 65.
22. Waters - The Science of What's Possible. *Waters- The Science of What's Possible*. [Online] [Cited: February 11, 2010.] www.waters.com.
23. Cullity, B.D. and Stock, S.R. *Elements of X-Ray Diffraction*. Upper Saddle River, NJ : Prentice Hall, 2001.
24. Flanders, P. J. An Alternating-Gradient Magnetometer. 1988, pp. 3940-3945.
25. David B. Williams, C. Barry Carter. *Transmission Electron Microscopy*. Springer, 2009.
26. Characterization, techniques, & instrumentation. *Nanomagnetics*. [Online] 2003. [Cited: June 14, 2009.] www.nanomagnetics.org.
27. Wang, L., et al. Model of ferromagnetic clusters in amorphous rare earth and transition metal alloys. 2001, Vol. 89, 12, pp. 8046-8053.
28. Fukagawa, Tomoki and Hirosawa, Satoshi. Influence of Nd/Nd₂Fe₁₄B interface microstructure on the coercivity of surface Nd₂Fe₁₄B grains in Nd-sputtered Nd-Fe-B sintered magnets. 2008, Vol. 59, pp. 183-186.
29. Tsubokawa, Yoshiyuki, Hirosawa, Satoshi and Shimizu, Ryuichi. Formation of "bcc Boundary Phase" in Transmission Electron Microscopy Samples of Nd-Fe-B Sintered Magnets. 1990, Vol. 30, 1, pp. 58-61.
30. Wnuk, Izabela, Wyslocki, Jerzy J. and Pryzbyl, Anna. Phase structure of the nanocrystalline Nd₂Fe₁₄B/ α -Fe magnets with different grain size. 2007, pp. 85-88.
31. Everts, J. *Concise encyclopedia of magnetic and superconducting materials*. Oxford : Pergamon Press, 1992.
32. Rui, X. and Shield, Jeffrey E. High-Energy Product Exchange-Spring FePt/Fe Cluster Nanocomposite Permanent Magnets. 2006, pp. 76-82.

33. Betancourt, I. and Davies, H.A. Exchange Coupled Nanocomposite Hard Magnetic Alloys. 2010, Vol. 26, 1, pp. 5-19.
34. Xirouchaki, C. and Palmer, E. Deposition of Size-Selected Metal Clusters Generated by Magnetron Sputtering and Gas Condensation: A Progress Review. 2003, pp. 117-124.
35. Siegel, R. W. Cluster-Assembled Nanophase Materials. 1991, pp. 559-578.
36. Makita, Ken and Yamashita, Osamu. Phase boundary structure in Nd-Fe-B sintered magnets. 1999, Vol. 74, 14, pp. 2056-2058.
37. Thomas, Luc, et al. Method, High-Sensitivity In-Plane Vector Magnetometry Using the Alternating Gradient Force. 2003, Vol. 93, 10, pp. 7062 - 7064.